Joule

CellPress
OPEN ACCESS

Article

Demonstration of ultrahigh thermoelectric efficiency of ~7.3% in Mg_3Sb_2/MgAgSb module for low-temperature energy harvesting

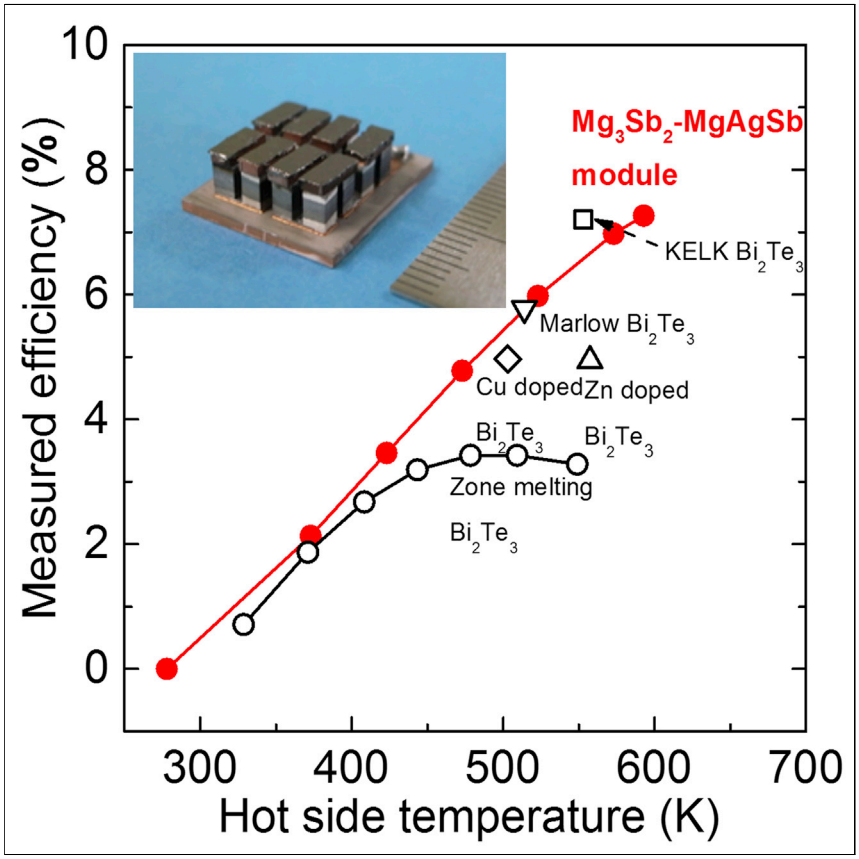

Thermoelectric harvesting of waste heat offers great opportunities for energy production. Here, we demonstrated that a minor Cu addition in the n-type $Mg_3Sb_{1.5}Bi_{0.5}$ realized the remarkable enhancement of low-temperature thermoelectric performance. Coupled with p-type α-MgAgSb, we fabricated a high-performance thermoelectric module, which showed a record-high conversion efficiency of 7.3% at the hot-side temperature of 593 K. Our module rivals the long-time champion Bi_2Te_3 in this applicably important temperature range, providing great promise for harvesting abundant low-grade waste heat.

Zihang Liu, Naoki Sato, Weihong Gao, ..., Jangho Yi, Koichi Tsuchiya, Takao Mori

mori.takao@nims.go.jp

Highlights

Cu addition in $Mg_3Sb_{1.5}Bi_{0.5}$ led to anomalously low thermal conductivity

High carrier mobility, comparable with a single crystal, was simultaneously obtained

An 8-pair $Mg_3Sb_{1.5}Bi_{0.5}$/MgAgSb thermoelectric module was successfully fabricated

Our module showed high efficiency of 7.3% at the hot-side temperature of 593 K

Liu et al., Joule 5, 1–13
May 19, 2021
https://doi.org/10.1016/j.joule.2021.03.017

Please cite this article in press as: Liu et al., Demonstration of ultrahigh thermoelectric efficiency of ~7.3% in Mg_3Sb_2/MgAgSb module for low-temperature energy harvesting, Joule (2021), https://doi.org/10.1016/j.joule.2021.03.017

Joule

CellPress
OPEN ACCESS

Article

Demonstration of ultrahigh thermoelectric efficiency of ~7.3% in Mg_3Sb_2/MgAgSb module for low-temperature energy harvesting

Zihang Liu,[1,7] Naoki Sato,[1,7] Weihong Gao,[1,7] Kunio Yubuta,[2] Naoyuki Kawamoto,[1] Masanori Mitome,[1] Keiji Kurashima,[3] Yuka Owada,[3] Kazuo Nagase,[4] Chul-Ho Lee,[4] Jangho Yi,[5] Koichi Tsuchiya,[5,6] and Takao Mori[1,6,8,*]

SUMMARY

Thermoelectric harvesting of low-temperature waste heat offers great opportunities for sustainable energy production. However, the investigations of related thermoelectric materials and modules remain sluggish. Here, we reported a great advance in the n-type $Mg_3Sb_{1.5}Bi_{0.5}$ system by minor Cu additions. Some Cu atoms preferentially occupy interstitial sites within the Mg_3Sb_2 lattice and significantly modified phonon modes via filling in the phonon gap and increased anharmonic phonon scattering, thereby leading to the anomalously low thermal conductivity. Simultaneously, the detrimental behavior of thermally activated electrical conductivity was completely eliminated through grain-boundary complexion engineering. These two critical roles contributed to the remarkable improvement of *zT*. Based on this developed high-performance material coupled with p-type α-MgAgSb-based material, a fabricated thermoelectric module rivaling long-time champion Bi_2Te_3, demonstrated a record-high conversion efficiency ~7.3% at the hot-side temperature of 593 K. These results pave the way for low-temperature thermoelectric harvesting.

INTRODUCTION

In the context of increased energy consumption and global environmental degradation, developing clean and sustainable energy-conversion technologies has received significant attention from both academic and industrial communities.[1] Thermal energy harvesting, which captures waste heat or natural heat and converting it to mechanical or electrical energy, provides the opportunity to utilize the ubiquitous heat sources for energy production.[2] Based on a reference temperature of 25°C, approximately 90% of waste heat is below 316°C.[3] For this low-grade heat source it is, however, uneconomic for waste-heat recovery using the traditional Rankine cycle, pushing researchers looking for other alternative technologies,[2] including thermoelectric, pyroelectric, thermomagnetic, and thermoelastic effect. Among them, thermoelectric technology is believed to be the most promising approach for power generation,[4,5] as it can directly convert the temperature gradient to electricity. The efficiency of thermoelectric power generation (TEG) is dominated by the dimensionless thermoelectric figure of merit (zT) is defined as $zT = [S^2\sigma/(\kappa_{lat} + \kappa_{ele})]T$, where S, σ, κ_{lat}, κ_{ele}, and T are Seebeck coefficient, electrical conductivity, lattice thermal conductivity, electronic thermal conductivity, and absolute temperature, respectively. Over the past two decades, we have witnessed tremendous advances in the of synthesis high-performance thermoelectric materials

Context & scale

Based on a reference temperature of 25°C, approximately 90% of waste heat is below 316°C. However, it is uneconomic for waste-heat recovery using the traditional Rankine cycle. Thermoelectric technology provides a promising approach for harvesting this low-grade heat. Herein, we report a great advance in the n-type $Mg_3Sb_{1.5}Bi_{0.5}$ system by a minor Cu addition, ranging from material design to module development. Thermal conductivity was suppressed due to the increased phonon-phonon scattering, while the thermally activated electrical conductivity was eliminated through grain-boundary complexion engineering. Coupled with p-type α-MgAgSb, a fabricated 8-pair thermoelectric module demonstrated a record-high conversion efficiency of ~7.3% at the hot-side temperature of 320°C (593 K). Our module enables a non-Bi_2Te_3-type material module to achieve such thermoelectric conversion performance to rival the long-time champion in this applicably important temperature range.

Please cite this article in press as: Liu et al., Demonstration of ultrahigh thermoelectric efficiency of ~7.3% in Mg_3Sb_2/MgAgSb module for low-temperature energy harvesting, Joule (2021), https://doi.org/10.1016/j.joule.2021.03.017

with zT close to or above 2, owing to efficient design concepts and/or advanced synthesis methods.[6–8] However, most high-zT candidates, e.g., lead chalcogenides,[9–11] filled $CoSb_3$,[12,13] SnSe crystal,[14,15] and half-Heusler alloys,[16–18] work in the medium- and high-temperature ranges. In this scenario, Bi_2Te_3-related materials that were discovered a half century ago still dominate the market for the low-temperature range applications,[19] usually limiting the maximum temperature below 200°C.

Recently, the discovery of high-performance n-type Mg_3Sb_2-based materials provides new hope for the replacement of traditional Bi_2Te_3.[20–23] Mg_3Bi_2 alloying not only reduces the band gap and band effective mass but also strengthens phonon scattering,[23–26] leading to a peak zT around 1.5–1.7 at over 700 K. Currently, most of the research activities focused on the nominal composition of $Mg_{3.2}Sb_{1.5}Bi_{0.5}$ for medium-temperature power generation, e.g., doping with chalcogens and/or transition metals,[27–30] as well as tuning the sintering temperature.[31,32] One interesting but detrimental behavior in $Mg_{3.2}Sb_{1.5}Bi_{0.5}$ systems is the thermally activated electrical conductivity in the low-temperature range, but the related origin remains ambiguous.[25,27–29,32] Therefore, the low-temperature properties are still inferior in comparison with n-type Bi_2Te_3. In addition, no studies about the fabrication of Mg_3Sb_2 thermoelectric module have been reported to date, only the single leg for power generation and a unicouple consisting of n-type Mg_3Sb_2 and p-type Bi_2Te_3 for cooling applications.[33–35]

Current strategies to enhance thermoelectric performance mainly include carrier-concentration optimization, point-defect scattering, as well as band structure and microstructure modification.[6] Beyond these conventional ideas, herein we discover two key enhancement components manifested by minor Cu addition in $Mg_{3.2}Sb_{1.5}Bi_{0.5}$, i.e., interstitial doping and grain-boundary complexions engineering, which are highlighted in Figure 1A. First, part of the doped Cu atoms preferentially occupied interstitial sites within the Mg_3Sb_2 lattice, which leads to filling in of the phonon gap, strengthening the anharmonic scattering, and thereby suppressing the thermal conductivity. Second, the Mg–Cu binary eutectic reaction induced the abnormal grain coarsening, the suppression of Mg evaporation during the sintering process, and the *in situ* formation of metallic phases located at the triple junction. This modification of grain-boundary complexions helps to eliminate the thermally activated electrical conductivity and contribute to the ultrahigh carrier mobility comparable with a single crystal.[36] Benefiting from these two aspects, zT has been significantly increased from 0.2 to 0.6 at room temperature while the peak zT at 773 K increased from 1.5 to 1.9 (Figure 1B), outperforming most of current n-type medium- and high-temperature materials.[10,12,37,38] Around room temperature range, our optimized material is even comparable to these Bi-rich n-type $Mg_3(Sb, Bi)_2$, namely, $Mg_{3.2}Sb_{0.5}Bi_{1.5}$ and $Mg_{3.2}Sb_{0.4}Bi_{1.4}$.[34,39] More importantly, we successfully fabricated, for the first time, the 8-pair thermoelectric module consisting of n-type $Mg_{3.2}Sb_{1.5}Bi_{0.49}Te_{0.01}Cu_{0.01}$ and p-type $Mg_{0.99}Cu_{0.01}Ag_{0.97}Sb_{0.99}$ for low-temperature power generation (Figure 1C, inset). The measured conversion efficiency reaches 7.3% at the hot-side temperature of 593 K (Figure 1C), as a record-high value in comparison to other advanced single-stage thermoelectric modules.[18,40–45] In addition, the output power density, determined by the output power divided by the cross-sectional area of the module substrate, is comparable with these advanced Bi_2Te_3 modules from laboratory and company (Figure 1D).[40–43] The module performance was tested for five times and showed the similar value with no deterioration (Figure S1). The demonstration of high efficiency coupled with high output power density in the Mg_3Sb_2/MgAgSb thermoelectric module provides great promise for harvesting abundant low-grade waste heat.

[1]WPI Center for Materials Nanoarchitectonics (WPI-MANA), National Institute for Materials Science (NIMS), Namiki 1-1, Tsukuba 305-0044, Japan

[2]Institute for Materials Research, Tohoku University, Katahira 2-1-1, Sendai 980-8577, Japan

[3]Research Network and Facility Services Division, National Institute for Materials Science (NIMS), Namiki 1-1, Tsukuba 305-0044, Japan

[4]National Institute of Advanced Industrial Science and Technology (AIST), Tsukuba, Ibaraki 305-8568, Japan

[5]Research Center for Structural Materials, National Institute for Materials Science, Tsukuba, Ibaraki 305-0047, Japan

[6]Graduate School of Pure and Applied Sciences, University of Tsukuba, Tennodai 1-1-1, Tsukuba 305-8671, Japan

[7]These authors contributed equally

[8]Lead contact

*Correspondence: mori.takao@nims.go.jp

https://doi.org/10.1016/j.joule.2021.03.017

Please cite this article in press as: Liu et al., Demonstration of ultrahigh thermoelectric efficiency of ~7.3% in Mg_3Sb_2/MgAgSb module for low-temperature energy harvesting, Joule (2021), https://doi.org/10.1016/j.joule.2021.03.017

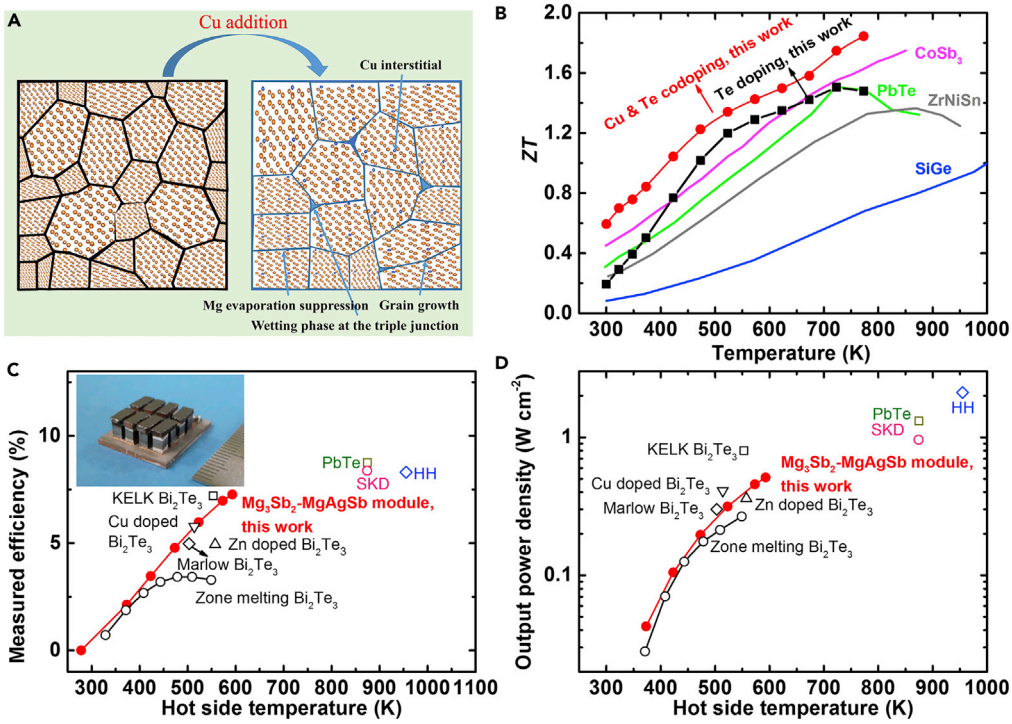

Figure 1. High-performance $Mg_{3.2}Sb_{1.5}Bi_{0.49}Te_{0.01}Cu_{0.01}$ thermoelectric materials and modules

(A) The schematic diagram of two related mechanisms of minor Cu addition in $Mg_{3.2}Sb_{1.5}Bi_{0.5}$.

(B) Temperature-dependent zTs of both $Mg_{3.2}Sb_{1.5}Bi_{0.49}Te_{0.01}$ and $Mg_{3.2}Sb_{1.5}Bi_{0.49}Te_{0.01}Cu_{0.01}$ in comparison with the state-of-the-art n-type thermoelectric materials, including PbTe,[10] $CoSb_3$ nanocomposite,[12] (Zr, Hf)NiSn,[37] and SiGe.[38]

(C and D) The measured conversion efficiency and output power density of 8-pair thermoelectric modules as a function of hot-side temperature, respectively, in comparison with modules of zone-melting Bi_2Te_3,[40] Zn-doped Bi_2Te_3,[40] Cu-doped Bi_2Te_3,[41] commercial Bi_2Te_3 from Marlow and KELK,[42,43] filled $CoSb_3$ (SKD),[45] PbTe,[44] and half-Heusler alloys (HH).[18]

RESULTS AND DISCUSSION

Mg_3X_2 (X = Sb and Bi), crystallizing in the inverse α-La_2O_3 structure, consists of two unique Mg Wyckoff positions.[23] In addition to which there are also some favorable interstitial sites for excess Mg or foreign dopant with small atomic radii. Based on the previous defect-formation energy calculations about interstitial insertion under Mg-rich conditions, it was revealed that interstitial Cu exhibited the lowest formation energy as the Fermi level E_f approached the conduction band minima (CBM).[46] Experimentally, based on the powder X-ray diffraction (XRD) refinement analysis (Figure S2), it was revealed that the minor addition of Cu in $Mg_{3.2}Sb_{1.5}Bi_{0.49}Te_{0.01}Cu_x$ does not significantly affect the lattice parameters a and c (Figure S3). Subsequently, using density functional theory (DFT) calculations, the most energetically stable interstitial site was determined (Figure 2A, visualized with VESTA 3). We find here that interstitial Cu in Mg_3Sb_2 enables the favorable modification of phonon structure for impeding heat transport through increasing the 3-phonon scattering. The phonon dispersion and phonon density of states (DOS) of pristine Mg_3Sb_2 reveals that both transverse acoustic phonon modes and optical modes are anomalously soft (Figure S4)[47] and responsible for the intrinsically low κ_{lat} of Mg_3Sb_2. Besides, a gap-like structure around 5 THz is clearly observed for the phonon DOS of Mg_3Sb_2 (Figure S4). According to the previous stimulation of κ_{lat} as a function of phonon frequency, high-frequency optical phonons from 5 THz to 9 THz show the nonnegligible contribution to thermal transport,[21] which is attributed to the absence of optical phonon-phonon scattering

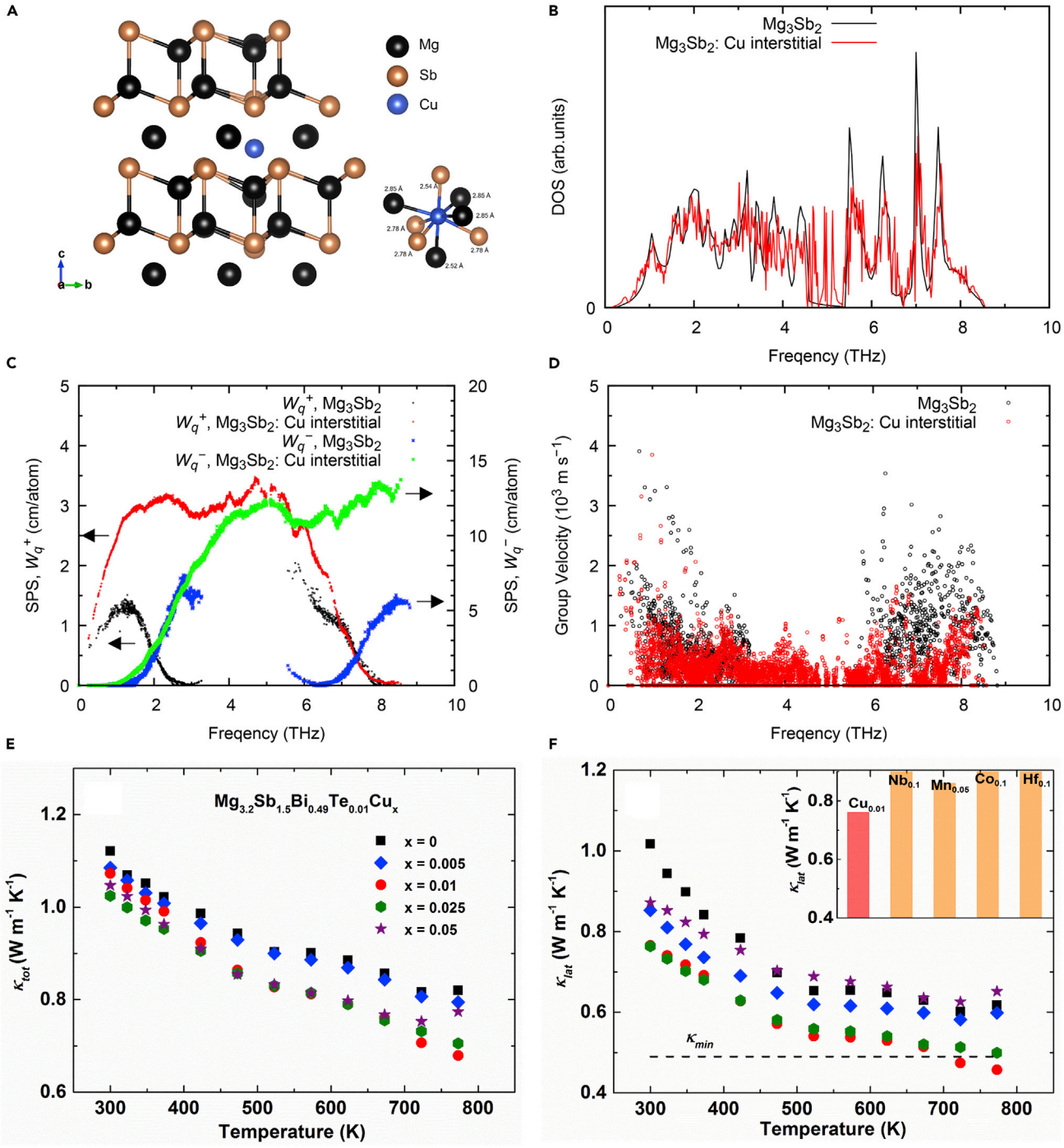

Figure 2. Thermal properties of $Mg_{3.2}Sb_{1.5}Bi_{0.49}Te_{0.01}Cu_x$

(A) The most energetically stable interstitial site within the Mg_3Sb_2 lattice.

(B–D) Comparison of the calculated phonon DOS, 3-phonon scattering-phase space, phonon-group velocity of Mg_3Sb_2 and Mg_3Sb_2 with interstitial Cu, respectively.

(E and F) Measured total thermal conductivity κ_{tot} and lattice thermal conductivity κ_{lat} of $Mg_{3.2}Sb_{1.5}Bi_{0.49}Te_{0.01}Cu_x$ (x = 0, 0.005, 0.01, 0.025, and 0.05). The dashed line represents the theoretical minimum κ_{lat} value and the inset compares the room-temperature κ_{lat} in $Mg_{3.2}Sb_{1.5}Bi_{0.5}$ system.[27–29]

Please cite this article in press as: Liu et al., Demonstration of ultrahigh thermoelectric efficiency of ~7.3% in Mg_3Sb_2/MgAgSb module for low-temperature energy harvesting, Joule (2021), https://doi.org/10.1016/j.joule.2021.03.017

channels in the gap region and large optical phonon-group velocity. On the other hand, interstitial Cu can insert some additional states within the gap region (Figure 2B), which results in a significant increase of a possible scattering channel. The calculated 3-phonon scattering-phase space (Figure 2C), which is a measure of the number of scattering channels satisfying energy and momentum conservation, suggests that interstitial Cu can not only increase the channel for the overall frequency region but can also insert the additional channel into the gap region existing in pristine Mg_3Sb_2. Simultaneously, interstitial Cu decreases the high-frequency optical phonon-group velocity (Figure 2D). These features significantly reduce the previously reported contribution of optical phonons to thermal transport. Experimentally, the minor addition of Cu induces the reduction of the total thermal conductivity κ_{tot} (Figure 2E). After calculating the Lorenz number L and extracting the electronic thermal conductivity κ_{ele} from κ_{tot}, the obtained κ_{lat} is remarkably suppressed after minor Cu addition (Figure 2F), even approaching the minimum κ_{lat} value at the high-temperature range. For instance, the κ_{lat} of $Mg_{3.2}Sb_{1.5}Bi_{0.49}Te_{0.01}Cu_{0.01}$ shows a reduction of 20%–30% over the entire temperature range in comparison to the pristine sample; that is, room-temperature κ_{lat} reduces from 1.04 W m^{-1} K^{-1} to 0.75 W m^{-1} K^{-1}. In addition, κ_{lat} of the minor Cu addition (1 at%) sample is apparently lower than other heavily doped samples with transition metals (Figure 2F, inset).[27–29] Therefore, this anomalous reduction of κ_{lat} after Cu addition is beyond the conventional expectation. It should be noted that the increased κ_{lat} of $Mg_{3.2}Sb_{1.5}Bi_{0.49}Te_{0.01}Cu_{0.05}$ is related to the abnormal grain growth that leads to the reduced grain-boundary scattering. Based on the aforementioned DFT calculations, this striking behavior is due to the modification of phonon structure, i.e., filling in the gap of phonon DOS, thereby reducing the phonon-group velocity and increasing the 3-phonon scattering rate. It should be noted that interstitial doping in thermoelectric has hitherto been usually utilized to increase the point-defect scattering[48] or to realize the optimum temperature-dependent carrier concentration.[49]

Experimentally, we employed Raman spectroscopy to get an insight into the vibrational properties. The Raman spectrum of Cu-free sample was consistent with a previous report,[50] while Cu addition lowers the signal intensity and, more importantly, the emergence of a broad peak (Figure S5). This remarkable change is related to the stronger lattice disorder and also the increased phonon DOS after Cu addition. In addition, sound-velocity measurement and low-temperature heat capacity measurements are also performed for $Mg_{3.2}Sb_{1.5}Bi_{0.49}Te_{0.01}$ and $Mg_{3.2}Sb_{1.5}Bi_{0.49}Te_{0.01}Cu_{0.01}$. The room-temperature sound velocity measured by using a sing-around ultrasonic velocity method, as well as these calculated parameters (the Debye temperature Θ_D and the Grüneisen parameter γ) determined from sound-velocity data, are displayed in Table S1. Both sound velocity and Debye temperature, as indicators of chemical bonding strength, show a reduction after Cu addition, which are consistent with our previous phonon calculations. The low-temperature heat capacity C_p from 3 to 20 K was measured, shown as C_p/T^3 as a function of T (Figure S6). A typical hump, meaning the excess contribution to the conventional Debye density of states (DOS), was observed for both samples, which is known as the ''boson peak.''[51] In terms of crystalline solids, this phenomenon is associated with these low-lying optical modes.[51] Since the experimental C_p/T^3 data show a strong deviation from the Debye model, the Debye-Einstein model with a different number of oscillators was further utilized for fitting, shown in Equation 1:

$$C_p/T = \delta + \beta T^2 + \sum_{i=1}^{n} A_i(\Theta_{Ei}) 2 \cdot \left(T^2\right)^{-3/2} \cdot \frac{e^{\Theta_{Ei}/T}}{\left(e^{\Theta_{Ei}/T} - 1\right)^2} \qquad \text{(Equation 1)}$$

Please cite this article in press as: Liu et al., Demonstration of ultrahigh thermoelectric efficiency of ~7.3% in Mg_3Sb_2/MgAgSb module for low-temperature energy harvesting, Joule (2021), https://doi.org/10.1016/j.joule.2021.03.017

where the first term is the electron contribution, in which δ is the Sommerfeld constant, the second term is the Debye lattice contribution, and the final term is related to the Einstein oscillator at the specific Einstein temperature Θ_{Ei}. Herein, upon introducing three Einstein oscillators, the data show the perfect fitting. The fitting parameters for these models were displayed in Table S2. The existence of the Einstein oscillator indicates the strong coupling between acoustic phonons and low-frequency optical phonons. By the comparison of model-fitting parameters of these two samples, the larger β value of $Mg_{3.2}Sb_{1.5}Bi_{0.49}Te_{0.01}Cu_{0.01}$ accounts for the higher Debye temperature than $Mg_{3.2}Sb_{1.5}Bi_{0.49}Te_{0.01}$, in good agreement with previous sound-velocity measurements. In addition, these slightly lower Θ_{Ei} values of $Mg_{3.2}Sb_{1.5}Bi_{0.49}Te_{0.01}Cu_{0.01}$ mean the lower frequency of quasi-localized optical phonon modes.

A previous report only focused on the carrier-concentration variation and concluded that Cu interstitial may be not an effective n-type dopant for Mg_3Sb_2.[46] In our work, the slightly increased carrier concentration n_H by 10% means that Cu atoms act as weak electron donors (Figure S7), which is another good indicator of Cu atoms locating at interstitial sites. This can be further proved by electron-localization-function (ELF) images that helps in understanding the electron localization in this system (Figure S8). The ELF around interstitial Cu shows low value and isotropic ionic features, suggesting that Cu interstitial acts as a donor. In contrast, n_H of the $x = 0.05$ sample decreases to half value of the pristine sample. It indicates that beyond the solid solubility at the interstitial sites, some of the remaining Cu atoms become the substitutional solutes on the Mg site and thereby lead to the reduced n_H.

For $Mg_{3.2}Sb_{1.5}Bi_{0.49}Te_{0.01}$, there is a characteristic behavior of the thermally activated electrical conductivity in the low-temperature range (Figure 3A), which is a common phenomenon in n-type Mg_3Sb_2 systems; however, its physical origin is still an ongoing and obscure discussion. Initially, this is ascribed to the ionized impurity scattering because utilizing some heavily doped transition metals, *e.g.*, Nb,[28] Co,[27] and Mn[29] weakened the corresponding scattering behavior and indicated that these foreign dopants may fill in the existing Mg vacancies in the lattice. However, no detailed microstructure investigations were performed after extrinsic doping in previous reports. Some following studies claimed that this behavior was due to the grain-boundary scattering effect since samples with the larger grain size (~30 μm) and Te-doped Mg_3Sb_2 single crystal show the absence of the signature of ionized impurity scattering.[32,52] It should be noted that sintering at high temperature or utilization of Mg vapor-saturation annealing process may substantially alter the concentration of Mg vacancies at the equilibrium state concurrently.

Herein, we found that the minor addition of Cu (1 at %) completely eliminates the extra scattering mechanism, resulting in the observed ideal acoustic phonon scattering. Samples with Cu addition ($x < 0.05$) show slightly higher carrier concentration but much larger carrier mobility (more than double) simultaneously in comparison with the pristine sample. Therefore, it can be concluded that the record-high carrier mobilities achieved in samples with Cu addition is not dominated by the carrier concentration variation, but benefits from the removal of extra scattering events. In addition, the effect of carrier-carrier scattering at room temperature can be generally neglected in semiconductors. μ_H values in the range of 117–173 $cm^2\ V^{-1}\ s^{-1}$ in our materials are considerably higher than those of the polycrystalline samples doped with transition metals and even surpass the single-crystal measured value (Figure 3B).[36] The obvious drop of electrical conductivity σ of the $x = 0.05$ sample is attributed to the compensating effect of Cu substitution on the Mg site.

Please cite this article in press as: Liu et al., Demonstration of ultrahigh thermoelectric efficiency of ~7.3% in Mg_3Sb_2/MgAgSb module for low-temperature energy harvesting, Joule (2021), https://doi.org/10.1016/j.joule.2021.03.017

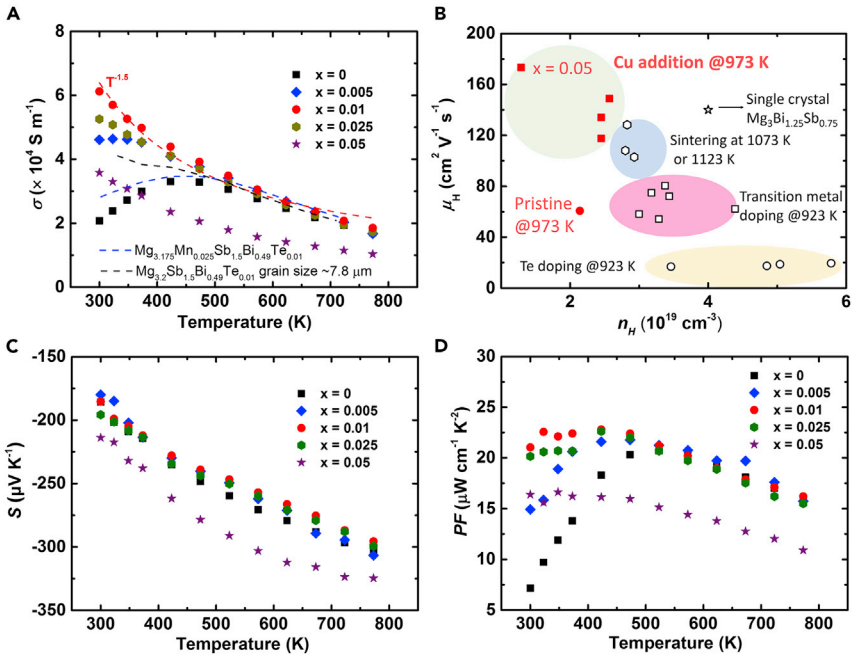

Figure 3. Electrical transport properties of $Mg_{3.2}Sb_{1.5}Bi_{0.49}Te_{0.01}Cu_x$ (x = 0, 0.005, 0.01, 0.025, and 0.05)

(A) Temperature-dependent σ of $Mg_{3.2}Sb_{1.5}Bi_{0.49}Te_{0.01}Cu_x$ in comparison with Mn- and Te-co-doped sample and sample with grain size of 7.8 μm. The red dashed line represents the theoretical value with the acoustic phonon scattering.

(B) The relationship between carrier concentration n_H and μ_H in $Mg_3Sb_{1.5}Bi_{0.5}$ systems, including Te doping,[28] co-doping with Te and transition metals,[27–29] coarse-grain samples by higher sintering temperature,[31,32] single crystal,[36] and our $Mg_{3.2}Sb_{1.5}Bi_{0.49}Te_{0.01}Cu_x$ samples.

(C and D) Temperature-dependent Seebeck coefficient S and power factor PF, respectively.

After Cu addition, the Seebeck coefficients S show negligible change due to the comparable carrier concentration except for the x = 0.05 sample (Figure 3C). In order to clarify the subtle variation of the Seebeck coefficient, the Pisarenko plot under the assumption of the single-parabolic-band (SPB) model with acoustic phonon scattering was calculated. All the experimental data lie around the line of total effective mass equal to 1.05 m_0 (Figure S9), where m_0 is the free-electron mass. This observation is consistent with our electronic band-structure calculations, in which interstitial Cu does not significantly affect the conduction-band structure around the Fermi level (Figure S10). Owing to the successful manipulation of the carrier-scattering mechanism after Cu addition, we can observe a significant enhance of the low-temperature power factor $PF = S^2\sigma$ (Figure 3D), which critically determines the potential of thermoelectric-module output power. For instance, the room-temperature PF has been increased from 7.2 to 21.1 μW cm^{-1} K^{-2}, an enhancement of approximately 3-fold.

To investigate the effect of grain-boundary scattering in our case, grain sizes were measured by electron backscatter diffraction (EBSD). After using the clean-up procedure, specifically, the average grain size of pristine and x = 0.01 samples was around 3.2 and 4.6 μm, respectively (Figures 4A and 4B). Furthermore, these scanning electron microscopy (SEM) images of fresh fracture surfaces also reveal the abnormal grain growth after Cu addition (Figure S11). This is related to the liquid-phase sintering due to the presence of Mg–Cu wetting liquid.[53] Excess Mg reacts with extrinsic Cu during the sintering process at 973 K since there is a Mg–Cu binary eutectic reaction at 758 K in the

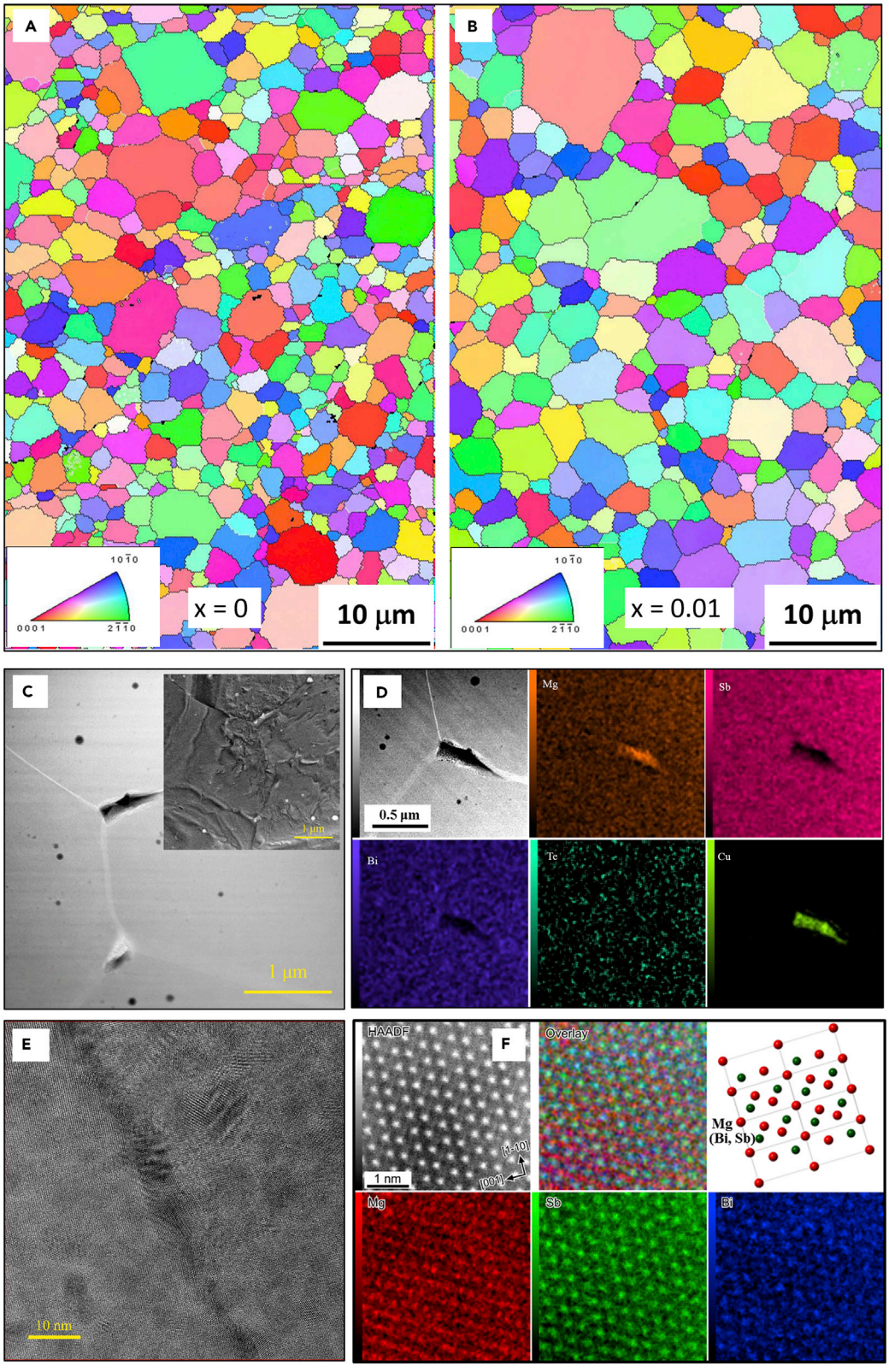
A
B
x = 0
10 μm
x = 0.01
10 μm
C
1 μm
1 μm
D
0.5 μm
Mg
Sb
Bi
Te
Cu
E
10 nm
HAADF
F
1 nm
Overlay
Mg
(Bi, Sb)
Mg
Sb
Bi

Please cite this article in press as: Liu et al., Demonstration of ultrahigh thermoelectric efficiency of ~7.3% in Mg_3Sb_2/MgAgSb module for low-temperature energy harvesting, Joule (2021), https://doi.org/10.1016/j.joule.2021.03.017

Figure 4. Microstructural evolution after minor Cu addition in $Mg_{3.2}Sb_{1.5}Bi_{0.49}Te_{0.01}$

(A and B) Comparison of EBSD images of $Mg_{3.2}Sb_{1.5}Bi_{0.49}Te_{0.01}$ and $Mg_{3.2}Sb_{1.5}Bi_{0.49}Te_{0.01}Cu_{0.01}$ samples, respectively.

(C) HADDF-STEM image showing the triple-junction regions with different contrast; inset is the corresponding TEM image.

(D) The corresponding HADDF-EDS mapping of the local area.

(E) HRTEM image around the grain boundary.

(F) Atomic-resolution HAADF-EDS mapping taken with the incident beam parallel to the [110] direction, together with the crystal structure model.

phase diagram (Figure S12). Both the low-magnification transmission electron microscopy (TEM) image and the scanning TEM (STEM) high-angle annular dark-field (HAADF) image show the grain size around several micrometers (Figure 4C), in agreement with previous EBSD results. A striking feature is the different contrast of the triple junction, indicating the occurrence of elemental segregation in this region. The corresponding energy dispersive X-ray spectroscopy (EDS) mapping reveals the character of both Mg- and Cu-rich in the area of the triple junction (Figure 4D), especially pronounced for the Cu element. Inside the grains, the low concentration of both Cu and Te results in the observed background noise. The triple junction shows the drag effect on the grain-boundary migration, whereas wetting-phase transformation contributes to the liquid-phase sintering and also abnormal grain growth.[54,55] On the basis of the composition analysis (Figure S13), this may prove the formation of the Mg_2Cu phase during the sintering process. In contrast, the HADDF-EDS mapping around the grain boundary reveals no segregation of Cu, but is observed with Bi segregation (Figure S14), consistent with a previous report.[29] This is a common character of n-type $Mg_3(Sb/Bi)_2$ systems, which has normally no or little correlation with the remarkable enhancement of thermoelectric performance after Cu addition. In terms of grain-boundary wetting-phase transitions, the liquid metal first occurs in the triple junctions and further penetrates into these adjacent grain boundaries. These wetting phases connecting to solid grains act as conductive channels of charge carriers, contributing to higher μ_H. Moreover, owing to the *in situ* formation mechanism, the resultant interfaces enable weaker carrier scattering in comparison to disordered grain boundaries. High density of nanoprecipitates can be observed in the high-resolution transmission electron microscopy (HRTEM) image around the grain boundary (Figure 4E) and inside the grain (Figure S15), which help to suppress phonon propagation to a certain extent. Atomic-resolution HAADF-EDS mapping yields the chemical homogeneity inside the grain. Unfortunately, due to the low concentration of Cu atoms and Te atoms below the detection limitation, the direct observation of these two atoms in STEM-HAADF image is currently impossible.

Moreover, the severe Mg evaporation in samples is beneficially suppressed thanks to this reaction of Mg and Cu occurring beforehand. First, the big difference of photos of graphite dies after sintering is the direct evidence (Figure S16). Second, the Mg stoichiometry is found to increase about 3% by analyzing the chemical composition of compacted disks by SEM + EDS (Table S3). As reported, approximately 5 at % of Mg deficiency is observed near grain boundaries using atom-probe tomography.[56] This may lead to the high resistance of grain boundaries due to a depletion of free electrons and potential barriers to conduction. In contrast, Cu addition helps to maximize the Mg stoichiometry along the grain boundaries, which should be effective to reduce grain-boundary resistance. To summarize, Cu addition was found to enable the control of the structure and chemistry of grain-boundary complexions, defined as the interfacial material in thermodynamic equilibrium with the abutting phases.[55] Benefiting from these triple modifications, the extra carrier-scattering mechanism is eliminated and record-high values of μ_H are obtained.

We should mention that the nearly isotropic three-dimensional bonding network in Mg_3Sb_2 excludes the chemical bonding as the physical origin of the increased

Please cite this article in press as: Liu et al., Demonstration of ultrahigh thermoelectric efficiency of ~7.3% in Mg_3Sb_2/MgAgSb module for low-temperature energy harvesting, Joule (2021), https://doi.org/10.1016/j.joule.2021.03.017

μ_H.[21,57] In terms of Mg vacancy concentration variation after Cu addition, this should be negligible, as the formation energy of Mg vacancies are positive at the Mg-rich condition when the Fermi level is near CBM.[46] The dielectric constant of the Mg_3Sb_2 system seems not to be sensitive to doping or alloying.[27] Besides, the calculated acoustic-deformation potential values, characterizing the coupling of electrons with acoustic phonons, are 10.334 and 10.656 eV, respectively, for pristine Mg_3Sb_2 and for interstitial Cu based on the DFT calculations. The small difference means that comparable electron-phonon coupling strength after the introduction of interstitial Cu. In a word, we can conclude that this extra scattering mechanism in n-type Mg_3Sb_2 is caused predominately by the grain-boundary scattering and, therefore, control of grain-boundary complexions offers the route for maximizing electrical transport properties.

To further prove the compositional and structural stability after Cu addition, we did the cycling test of electrical transport properties for the best composition—$Mg_{3.2}Sb_{1.5}Bi_{0.49}Te_{0.01}Cu_{0.01}$. Considering our research aim for the low-temperature waste-heat harvesting, the maximum temperature here is limited to 573 K. It is apparent that the material shows an excellent stability at this temperature range (Figure S17). As a consequence of increased *PF* and concurrently reduced κ_{tot}, Cu addition further largely enhances *zT*, especially for the low-temperature range. The highest average *zT* calculated by the integral method from 300 to 773 K is significantly boosted to 1.3, which is a record-high value in the $Mg_{3.2}Sb_{1.5}Bi_{0.5}$ system (Figure S18). Considering the thermal stability issue of n-type $Mg_3Sb_{2-x}Bi_x$ system,[58] the maximum measured temperature for the corresponding thermoelectric module was limited to 600 K, which covers the targeted temperature range of abundant waste heat. Pairing with a suitable p-type leg and fabricating the high-performance module are, however, challenging since so many critical factors—e.g., contact-layer design, as well as the assembly with electrodes and substrates—affect the real working performance in service. After searching for the currently available p-type thermoelectric materials, we judge that α-MgAgSb is the most promising p-type counterpart candidate for low-temperature power generation below 600 K.[59–62] This is due to the comparable coefficient of thermal expansion (CTE) (23.78×10^{-6} K for $Mg_{3.2}Sb_{1.5}Bi_{0.5}$ versus 20×10^{-6} K for α-MgAgSb), mechanical (Young's modulus: 42–45 GPa for $Mg_{3.2}Sb_{1.5}Bi_{0.5}$ versus 55 GPa for α-MgAgSb) and thermoelectric properties.[26,35,63,64] Using the similar synthesis method,[59,61] p-type $Mg_{0.99}Cu_{0.01}Ag_{0.97}Sb_{0.99}$ possesses a broad-temperature plateau of *zT* above 1 in which Cu doping enables the optimization of thermoelectric properties by tuning the carrier concentration (Figure S19). The critical phase-transition temperature from α-MgAgSb to β-MgAgSb is determined around 613 K by differential scanning calorimetry (DSC) analysis (Figure S20), below the module maximum measurement temperature. The sandwich-structure thermoelectric legs, including the thermoelectric elements and contact layer, were fabricated by the one-step sintering method, in which Fe and Ag powder were used as the contact layer for n-type and p-type material, respectively. The EDS mapping demonstrated no observable diffusion across the interfacial layer (Figures S21 and S22). The power generation characteristics of the fabricated module consisting of 8-couple p- and n-type legs were measured by the home-made system while the corresponding theoretical performance was evaluated by the home-made program (TEPS1D300). The details of module fabrication, testing, and stimulation can be found in the supporting information. The terminal voltage *V*, the electrical power output *P*, the heat dissipation from the cold side of the module Q_{out}, and the conversion efficiency η were displayed as functions of electric current *I* (Figure S23). We were able to obtain a striking module performance, attaining a record-high conversion efficiency ~7.3%, together with a high output power density of ~0.51 W cm^{-2} with the hot-side temperature of 593 K. However, the measured maximum *P* (P_{max}) and

maximum η (η_{max}) are 60%–70% of the stimulated counterpart (Figure S24). The measured open circuit voltage V_{oc} and maximum heat flow Q_{max} are in good agreement with the stimulation results, while the measured internal resistance R of thermoelectric module are 1.3–1.4 times higher (Figure S24). On the other hand, the overestimation of the calculation by ignoring the radiation heat exchange in the module must be less than 10%. The large R mainly arises from the relatively large interfacial resistance of both n-type and p-type legs (Figure S25). Future work needs to be done about interfacial layer design to solve this problem in order to achieve higher module performance.

Conclusions

In summary, we demonstrated the effectiveness of utilizing a minor Cu addition in substantially enhancing thermoelectric performance of n-type $Mg_{3.2}Sb_{1.5}Bi_{0.5}$. This is mainly attributed to the importance of both interstitial Cu in the lattice and grain-boundary complexions, which maximizes electrical transport properties and suppresses thermal conductivity synergistically. The resultant room-temperature and peak zTs were boosted to 0.6 and 1.9, respectively. When coupled with p-type α-MgAgSb-based material, a high-performance thermoelectric module was fabricated and exhibited for the first time a record-high conversion efficiency ~7.3% with the hot-side temperature of 593 K, which hold great promise for low-temperature thermal energy harvesting.

EXPERIMENTAL PROCEDURES

Resource availability

Lead contact

Further information and requests for resources and materials should be directed to and will be fulfilled by the Lead Contact, Takao Mori (MORI.Takao@nims.go.jp).

Materials availability

The materials in this study will be made available on request.

Data and code availability

The published article includes all data generated or analyzed during this study.

Full experimental procedures are provided in the Supplemental information.

SUPPLEMENTAL INFORMATION

Supplemental information can be found online at https://doi.org/10.1016/j.joule.2021.03.017.

ACKNOWLEDGMENTS

This work was supported by JST Mirai Program grant no. JPMJMI19A1 and JSPS KAKENHI JP17H02749, JP16H06441. The computation in this work has been performed using Numerical Materials Simulator at NIMS. Z. Liu acknowledges the financial support from the NIMS-MANA Postdoctoral Fellowship. C.H. Lee also thanks JST CREST grant number JPMJCR20Q4 for funding. K. Yubuta thanks JSPS KAKENHI grant number JP20H05258 for funding and thanks Akira Yasuhara, JEOL, for assistance with JEM-ARM200F observations.

AUTHOR CONTRIBUTIONS

Z.L. and T.M. developed the concept and designed the experiments. N.S. carried out the theoretical calculations. W.G., K.Y., N.K., M.M., K.K., and Y.O. performed the TEM observations and related analysis. Z.L., K.N., and C.L. made the

thermoelectric module and performed the measurement. J.Y. and K.T. performed the EBSD observation and analysis. T.M. supervised the whole project. All authors discussed the results and commented on the manuscript.

DECLARATION OF INTERESTS

T.M. and Z.L. have filed two Japanese patent applications (2020–151704 and 2020–155093) on the work described here.

Received: February 5, 2021
Revised: March 4, 2021
Accepted: March 23, 2021
Published: April 16, 2021

REFERENCES

1. Mori, T., and Priya, S. (2018). Materials for energy harvesting: at the forefront of a new wave. MRS Bull *43*, 176–180.

2. Kishore, R.A., and Priya, S. (2018). A review on low-grade thermal energy harvesting: materials, methods and devices. Materials (Basel) *11*, 1433.

3. Johnson, I., Choate, W.T., and Davidson, A. (2008). Waste Heat Recovery. Technology and Opportunities in US Industry. https://www1.eere.energy.gov/manufacturing/intensiveprocesses/pdfs/waste_heat_recovery.pdf.

4. Petsagkourakis, I., Tybrandt, K., Crispin, X., Ohkubo, I., Satoh, N., and Mori, T. (2018). Thermoelectric materials and applications for energy harvesting power generation. Sci. Technol. Adv. Mater. *19*, 836–862.

5. Shi, X.L., Zou, J., and Chen, Z.G. (2020). Advanced thermoelectric design: from materials and structures to devices. Chem. Rev. *120*, 7399–7515.

6. He, J., and Tritt, T.M. (2017). Advances in thermoelectric materials research: looking back and moving forward. Science *357*, eaak9997.

7. Mori, T. (2017). Novel principles and nanostructuring methods for enhanced thermoelectrics. Small *13*, 1702013.

8. Xiao, Y., and Zhao, L.D. (2020). Seeking new, highly effective thermoelectrics. Science *367*, 1196–1197.

9. Biswas, K., He, J.Q., Blum, I.D., Wu, C.I., Hogan, T.P., Seidman, D.N., Dravid, V.P., and Kanatzidis, M.G. (2012). High-performance bulk thermoelectrics with all-scale hierarchical architectures. Nature *489*, 414–418.

10. Xiao, Y., Wu, H.J., Li, W., Yin, M.J., Pei, Y.L., Zhang, Y., Fu, L.W., Chen, Y.X., Pennycook, S.J., Huang, L., et al. (2017). Remarkable roles of Cu to synergistically optimize phonon and carrier transport in n-Type PbTe-Cu2Te. J. Am. Chem. Soc. *139*, 18732–18738.

11. Wu, Y., Chen, Z., Nan, P., Xiong, F., Lin, S., Zhang, X., Chen, Y., Chen, L., Ge, B., and Pei, Y. (2019). Lattice strain advances thermoelectrics. Joule *3*, 1276–1288.

12. Zhao, W.Y., Liu, Z., Sun, Z., Zhang, Q.J., Wei, P., Mu, X., Zhou, H., Li, C., Ma, S., He, D., et al. (2017). Superparamagnetic enhancement of thermoelectric performance. Nature *549*, 247–251.

13. Khan, A.U., Kobayashi, K., Tang, D.-M., Yamauchi, Y., Hasegawa, K., Mitome, M., Xue, Y.M., Jiang, B.Z., Tsuchiya, K., Golberg, D., et al. (2017). Nano-micro-porous skutterudites with 100% enhancement in ZT for high performance thermoelectricity. Nano Energy *31*, 152–159.

14. Zhao, L.D., Tan, G.J., Hao, S.Q., He, J.Q., Pei, Y.L., Chi, H., Wang, H., Gong, S.K., Xu, H.B., Dravid, V.P., et al. (2016). Ultrahigh power factor and thermoelectric performance in hole-doped single-crystal SnSe. Science *351*, 141–144.

15. Lee, Y.K., Luo, Z., Cho, S.P., Kanatzidis, M.G., and Chung, I. (2019). Surface oxide removal for polycrystalline SnSe reveals near-single-crystal thermoelectric performance. Joule *3*, 719–731.

16. Fu, C.G., Bai, S.Q., Liu, Y.T., Tang, Y.S., Chen, L.D., Zhao, X.B., and Zhu, T.J. (2015). Realizing high figure of merit in heavy-band p-type half-Heusler thermoelectric materials. Nat. Commun. *6*, 8144.

17. Zhu, H.T., Mao, J., Feng, Z.Z., Sun, J.F., Zhu, Q., Liu, Z.H., Singh, D.J., Wang, Y.M., and Ren, Z.F. (2019). Understanding the asymmetrical thermoelectric performance for discovering promising thermoelectric materials. Sci. Adv. *5*, eaav5813.

18. Yu, J., Xing, Y., Hu, C., Huang, Z., Qiu, Q., Wang, C., Xia, K., Wang, Z., Bai, S., Zhao, X., et al. (2020). Half-Heusler thermoelectric module with high conversion efficiency and high power density. Adv. Energy Mater. *10*, 8144.

19. Poudel, B., Hao, Q., Ma, Y., Lan, Y.C., Minnich, A., Yu, B., Yan, X., Wang, D.Z., Muto, A., Vashaee, D., et al. (2008). High-thermoelectric performance of nanostructured bismuth antimony telluride bulk alloys. Science *320*, 634–638.

20. Pedersen, S.H. (2012). Thermoelectric properties of Zintl compounds Mg3Sb2-xBix, Department of Chemistry (Aarhus University). https://chem.au.dk/fileadmin/cmc.chem.au.dk/pictures_new_homepage/Pedersen_S_H_-_Thermoelectric_Properties_of_Zintl_Compounds_Mg3Sb2-xBix.pdf.

21. Tamaki, H., Sato, H.K., and Kanno, T. (2016). Isotropic conduction network and defect chemistry in Mg3+δSb2-based layered Zintl compounds with high thermoelectric performance. Adv. Mater. *28*, 10182–10187.

22. Zhang, J., Song, L., Pedersen, S.H., Yin, H., Hung, L.T., and Iversen, B.B. (2017). Discovery of high-performance low-cost n-type Mg3Sb2-based thermoelectric materials with multi-valley conduction bands. Nat. Commun. *8*, 13901.

23. Zhang, J., Song, L., and Iversen, B.B. (2019). Insights into the design of thermoelectric Mg3Sb2 and its analogs by combining theory and experiment. npj Comput. Mater. *5*, 76.

24. Shi, X., Zhao, T., Zhang, X., Sun, C., Chen, Z., Lin, S., Li, W., Gu, H., and Pei, Y. (2019). Extraordinary n-type Mg3SbBi thermoelectrics enabled by yttrium doping. Adv. Mater. *31*, e1903387.

25. Wood, M., Kuo, J.J., Imasato, K., and Snyder, G.J. (2019). Improvement of low-temperature zT in a Mg3Sb2-Mg3Bi2 solid solution via Mg-vapor annealing. Adv. Mater. *31*, e1902337.

26. Shu, R., Zhou, Y., Wang, Q., Han, Z., Zhu, Y., Liu, Y., Chen, Y., Gu, M., Xu, W., Wang, Y., et al. (2019). Mg3+δSbxBi2−x family: a promising substitute for the state-of-the-art n-type thermoelectric materials near room temperature. Adv. Funct. Mater. *29*, https://doi.org/10.1002/adfm.201807235.

27. Mao, J., Shuai, J., Song, S.W., Wu, Y., Dally, R., Zhou, J.W., Liu, Z.H., Sun, J.F., Zhang, Q.Y., dela Cruz, C., et al. (2017). Manipulation of ionized impurity scattering for achieving high thermoelectric performance in n-type Mg3Sb2-based materials. Proc. Natl. Acad. Sci. U. S. A. *114*, 10548–10553.

28. Shuai, J., Mao, J., Song, S.W., Zhu, Q., Sun, J.F., Wang, Y.M., He, R., Zhou, J.W., Chen, G., Singh, D.J., et al. (2017). Tuning the carrier scattering mechanism to effectively improve the thermoelectric properties. Energy Environ. Sci. *10*, 799–807.

29. Chen, X.X., Wu, H.J., Cui, J., Xiao, Y., Zhang, Y., He, J.Q., Chen, Y., Cao, J., Cai, W., Pennycook, S.J., et al. (2018). Extraordinary thermoelectric performance in n-type manganese doped

Mg3Sb2 Zintl: high band degeneracy, tuned carrier scattering mechanism and hierarchical microstructure. Nano Energy *52*, 246–255.

30. Song, S.W., Mao, J., Bordelon, M., He, R., Wang, Y.M., Shuai, J., Sun, J.Y., Lei, X.B., Ren, Z.S., Chen, S., et al. (2019). Joint effect of magnesium and yttrium on enhancing thermoelectric properties of n-type Zintl Mg3+δY0.02Sb1.5Bi0.5. Mater. . Today Phys. *8*, 25–33.

31. Mao, J., Wu, Y.X., Song, S.W., Zhu, Q., Shuai, J., Liu, Z.H., Pei, Y.Z., and Ren, Z.F. (2017). Defect engineering for realizing high thermoelectric performance in n-type Mg3Sb2-based materials. ACS Energy Lett *2*, 2245–2250.

32. Kanno, T., Tamaki, H., Sato, H.K., Kang, S.D., Ohno, S., Imasato, K., Kuo, J.J., Snyder, G.J., and Miyazaki, Y. (2018). Enhancement of average thermoelectric figure of merit by increasing the grain-size of Mg3.2Sb1.5Bi0.49Te0.01. Appl. Phys. Lett. *112*, 23102–23109.

33. Zhu, Q., Song, S.W., Zhu, H.T., and Ren, Z.F. (2019). Realizing high conversion efficiency of Mg3Sb2-based thermoelectric materials. J. Power Sources *414*, 393–400.

34. Mao, J., Zhu, H.T., Ding, Z.W., Liu, Z.H., Gamage, G.A., Chen, G., and Ren, Z.F. (2019). High thermoelectric cooling performance of n-type Mg3Bi2-based materials. Science *365*, 495–498.

35. Yin, L., Chen, C., Zhang, F., Li, X., Bai, F., Zhang, Z., Wang, X., Mao, J., Cao, F., Chen, X., et al. (2020). Reliable N-type Mg3.2Sb1.5Bi0.49Te0.01/304 stainless steel junction for thermoelectric applications. Acta Mater *198*, 25–34.

36. Pan, Y., Yao, M., Hong, X., Zhu, Y., Fan, F., Imasato, K., He, Y., Hess, C., Fink, J., Yang, J., et al. (2020). Mg3(Bi,Sb)2 single crystals towards high thermoelectric performance. Energy Environ. Sci. *13*, 1717–1724.

37. Kang, H.B., Poudel, B., Li, W., Lee, H., Saparamadu, U., Nozariasbmarz, A., Kang, M.G., Gupta, A., Heremans, J.J., and Priya, S. (2020). Decoupled phononic-electronic transport in multi-phase n-type half-Heusler nanocomposites enabling efficient high temperature power generation. Mater. Today *36*, 63–72.

38. Zebarjadi, M., Joshi, G., Zhu, G., Yu, B., Minnich, A., Lan, Y., Wang, X., Dresselhaus, M., Ren, Z., and Chen, G. (2011). Power factor enhancement by modulation doping in bulk nanocomposites. Nano Lett *11*, 2225–2230.

39. Imasato, K., Kang, S.D., and Snyder, G.J. (2019). Exceptional thermoelectric performance in Mg3Sb0.6Bi1.4 for low-grade waste heat recovery. Energy Environ. Sci. *12*, 965–971.

40. Deng, R., Su, X., Hao, S., Zheng, Z., Zhang, M., Xie, H., Liu, W., Yan, Y., Wolverton, C., Uher, C., et al. (2018). High thermoelectric performance in Bi0.46Sb1.54Te3 nanostructured with ZnTe. Energy Environ. Sci. *11*, 1520–1535.

41. Hao, F., Qiu, P., Tang, Y., Bai, S., Xing, T., Chu, H.-S., Zhang, Q., Lu, P., Zhang, T., Ren, D., et al. (2016). High efficiency Bi2Te3-based materials and devices for thermoelectric power generation between 100 and 300°C. Energy Environ. Sci. *9*, 3120–3127.

42. Marlow, I.-V. (2020). Thermoelectric generator (TEG) modules. https://ii-vicom/product/thermoelectric-generator-teg-modules/.

43. KELK Ltd. High Performance Type / Multi Purpose Type. https://www.kelk.co.jp/english/products/data_1.html#data_1_1, 2019

44. Hu, X., Jood, P., Ohta, M., Kunii, M., Nagase, K., Nishiate, H., Kanatzidis, M.G., and Yamamoto, A. (2016). Power generation from nanostructured PbTe-based thermoelectrics: comprehensive development from materials to modules. Energy Environ. Sci. *9*, 517–529.

45. Zong, P.A., Hanus, R., Dylla, M., Tang, Y.S., Liao, J.C., Zhang, Q.H., Snyder, G.J., and Chen, L.D. (2017). Skutterudite with graphene-modified grain-boundary complexion enhances zT enabling high-efficiency thermoelectric device. Energy Environ. Sci. *10*, 183–191.

46. Gorai, P., Ortiz, B.R., Toberer, E.S., and Stevanović, V. (2018). Investigation of n-type doping strategies for Mg3Sb2. J. Mater. Chem. A *6*, 13806–13815.

47. Peng, W., Petretto, G., Rignanese, G.-M., Hautier, G., and Zevalkink, A. (2018). An unlikely route to low lattice thermal conductivity: small atoms in a simple layered structure. Joule *2*, 1879–1893.

48. Pei, Y.Z., Zheng, L.L., Li, W., Lin, S.Q., Chen, Z.W., Wang, Y.Y., Xu, X.F., Yu, H.L., Chen, Y., and Ge, B.H. (2016). Interstitial point defect scattering contributing to high thermoelectric performance in SnTe. Adv. Electron. Mater. *2*, 3861–3870.

49. You, L., Zhang, J., Pan, S., Jiang, Y., Wang, K., Yang, J., Pei, Y., Zhu, Q., Agne, M.T., Snyder, G.J., et al. (2019). Realization of higher thermoelectric performance by dynamic doping of copper in n-type PbTe. Energy Environ. Sci. *12*, 3089–3098.

50. Bhardwaj, A., Shukla, A.K., Dhakate, S.R., and Misra, D.K. (2015). Graphene boosts thermoelectric performance of a Zintl phase compound. RSC Adv *5*, 11058–11070.

51. Takabatake, T., Suekuni, K., Nakayama, T., and Kaneshita, E. (2014). Phonon-glass electron-crystal thermoelectric clathrates: experiments and theory. Rev. Mod. Phys. *86*, 669–716.

52. Imasato, K., Fu, C., Pan, Y., Wood, M., Kuo, J.J., Felser, C., and Snyder, G.J. (2020). Metallic n-type Mg3Sb2 single crystals demonstrate the absence of ionized impurity scattering and enhanced thermoelectric performance. Adv. Mater. *32*, e1908218.

53. German, R.M., Suri, P., and Park, S.J. (2009). Review: liquid phase sintering. J. Mater. Sci. *44*, 1–39.

54. Gottstein, G., King, A.H., and Shvindlerman, L.S. (2000). The effect of triple-junction drag on grain growth. Acta Mater *48*, 397–403.

55. Cantwell, P.R., Tang, M., Dillon, S.J., Luo, J., Rohrer, G.S., and Harmer, M.P. (2014). Grain boundary complexions. Acta Mater *62*, 1–48.

56. Kuo, J.J., Yu, Y., Kang, S.D., Cojocaru-Mirédin, O., Wuttig, M., and Snyder, G.J. (2019). Mg Deficiency in Grain Boundaries of n-Type Mg3Sb2 Identified by Atom Probe Tomography. Adv. Mater. Interfaces *6*, 1900429.

57. Zhang, J., Song, L., Sist, M., Tolborg, K., and Iversen, B.B. (2018). Chemical bonding origin of the unexpected isotropic physical properties in thermoelectric Mg3Sb2 and related materials. Nat. Commun. *9*, 4716.

58. Imasato, K., Wood, M., Kuo, J.J., and Snyder, G.J. (2018). Improved stability and high thermoelectric performance through cation site doping in n-type La-doped Mg3Sb1.5Bi0.5. J. Mater. Chem. A *6*, 19941–19946.

59. Zhao, H.Z., Sui, J.H., Tang, Z.J., Lan, Y.C., Jie, Q., Kraemer, D., McEnaney, K., Guloy, A., Chen, G., and Ren, Z.F. (2014). High thermoelectric performance of MgAgSb-based materials. Nano Energy *7*, 97–103.

60. Ying, P.J., Liu, X.H., Fu, C.G., Yue, X.Q., Xie, H.H., Zhao, X.B., Zhang, W.Q., and Zhu, T.J. (2015). High performance α-MgAgSb thermoelectric materials for low temperature power generation. Chem. Mater. *27*, 909–913.

61. Liu, Z.H., Wang, Y.M., Mao, J., Geng, H.Y., Shuai, J., Wang, Y.X., He, R., Cai, W., Sui, J.H., and Ren, Z.F. (2016). Lithium doping to enhance thermoelectric performance of MgAgSb with weak electron-phonon coupling. Adv. Energy Mater. *6*, 1502269.

62. Liu, Z.H., Mao, J., Sui, J.H., and Ren, Z.F. (2018). High thermoelectric performance of α-MgAgSb for power generation. Energy Environ. Sci. *11*, 23–44.

63. Kraemer, D., Sui, J.H., McEnaney, K., Zhao, H.Z., Jie, Q., Ren, Z.F., and Chen, G. (2015). High thermoelectric conversion efficiency of MgAgSb-based material with hot-pressed contacts. Energy Environ. Sci. *8*, 1299–1308.

64. Liu, Z.H., Gao, W.H., Meng, X.F., Li, X.B., Mao, J., Wang, Y.M., Shuai, J., Cai, W., Ren, Z.F., and Sui, J.H. (2017). Mechanical properties of nanostructured thermoelectric materials α-MgAgSb. Scr. Mater. *127*, 72–75.

Joule, Volume *5*

Supplemental information

Demonstration of ultrahigh thermoelectric efficiency of ~7.3% in Mg_3Sb_2/MgAgSb module for low-temperature energy harvesting

Zihang Liu, Naoki Sato, Weihong Gao, Kunio Yubuta, Naoyuki Kawamoto, Masanori Mitome, Keiji Kurashima, Yuka Owada, Kazuo Nagase, Chul-Ho Lee, Jangho Yi, Koichi Tsuchiya, and Takao Mori

Materials and Methods

Materials Synthesis

High-purity raw materials from Sigma-Aldrich company were directly weighed according to the nominal composition $Mg_{3.2}Sb_{1.5}Bi_{0.49}Te_{0.01}Cu_x$ (x = 0, 0.005, 0.01, 0.025, and 0.05), as well as $Mg_{1-x}Cu_xAg_{0.97}Sb_{0.99}$ (x = 0 and 0.01), loaded into the stainless-steel ball milling jaw in the glovebox, and finally subjected to high-energy milling process. For $Mg_{3.2}Sb_{1.5}Bi_{0.49}Te_{0.01}Cu_x$, the ball-milling time is 5 hours and the obtained nanopowders were loaded into the graphite die and immediately sintered by spark plasma sintering (SPS, SPS-1080 System, SPS SYNTEX INC) at 973 K with the pressure of ~ 60 MPa for 5 min. In terms of synthesizing $Mg_{1-x}Cu_xAg_{0.97}Sb_{0.99}$, we used the two-step ball milling method[1,2] and then did SPS at 573 K to get the high-density disks.

Phase and microstructure characterizations

The phase structure were characterized by powder X-ray diffraction (XRD, SmartLab3, Rigaku) with Cu K_α radiation and further analyzed by Rietveld refinement method. The micro-Raman/PL was performed using a laser confocal microscope (inVia, Renishaw) with the 532-nm excitation laser and an electron multiplying CCD detector (Andor). Differential scanning calorimeter (DSC) measurement (Netzsch STA 449F1 Jupiter) in an N_2 atmosphere at a heating rate of 15 K/min was used to determine the phase transition temperature. The microstructure and composition analysis were characterized using a field emission scanning electron microscope (FESEM, Hitachi S-4800) equipped with an energy dispersive spectrometer (EDS, Horiba EMAXEvolution X-Max). Electron backscattered diffraction (EBSD) measurements were performed on a FE-SEM (JSM-7001F, JEOL Inc.) operated at 15 kV with the step size of 0.2 μm. These samples for EBSD observation are prepared by mechanical polishing to 3 μm with diamond paste and then ion milling (3 kV for 1-1.5 hours). Small pieces of cross sectional TEM (X-TEM) sample were prepared by focused ion beam (FIB) (Hitachi FB-2000S) method for TEM observation using a beam of focused high-energy (30 kV)

gallium ions. Scanning Transmission electron microscopy (STEM) characterization as well as EDS analysis were performed using a double-corrected JEM-ARM300F operated at 300 keV. The atomic resolution STEM image were taken on a JEOL JEM-ARM200F microscope with spherical aberration (Cs) corrector for the electron probe, using an accelerating voltage of 200 kV. Thin TEM specimens were prepared by Ar ion milling and focused ion beam (FIB) methods.

Material property characterizations

Bar samples were cut from the pressed disks and used for simultaneous measurement of electrical resistivity (ρ) and Seebeck coefficient (S) on a commercial system (ULVAC ZEM-2). The thermal conductivity κ_{tot} was calculated using $\kappa_{tot} = DC_pd$, where D, C_p, and d are the thermal diffusivity, specific heat capacity, and density, respectively. The thermal diffusivity coefficient (D) and the specific heat capacity (C_p) were concurrently measured for the disk sample on a laser flash system (Netzsch LFA 467, Germany) with a pyroceram disk as a reference sample. The sample density (d) was determined by the Archimedes method. The room-temperature Hall coefficient R_H was measured using the PPMS (Physical Properties Measurement System, Quantum Design) with the AC transport option. The data were obtained with a magnetic field sweeping from -5 T to +5 T. The Hall carrier concentration (n_H) was obtained by $n_H = 1/eR_H$ and the Hall carrier mobility (μ_H) was calculated by $\sigma = e\mu_H n_H$, where e is the electronic charge and σ the electrical conductivity. The low-temperature heat capacity was measured using PPMS (Physical Properties Measurement System, Quantum Design). The room-temperature sound velocity measurement was performed by using a sing-around ultrasonic velocity measuring instrument Model UVM-2, Ultrasonic Engineering Co., Ltd.

Module fabrication and characterization

Thermoelectric legs of n-type $Mg_{3.2}Sb_{1.5}Bi_{0.49}Te_{0.01}Cu_{0.01}$ and p-type $Mg_{0.99}Cu_{0.01}Ag_{0.97}Sb_{0.99}$ legs with contact layer were fabricated by the one-step SPS using the same condition with previously mentioned. Fe powder and Ag powder for n-type and p-type contact layer were used as the starting material, respectively. These

obtained sandwich disks were grinding, polishing, and dicing. The cross section of legs is 2.0 mm × 2.0 mm with a total length 3 mm. The lengths of the thermoelectric elements and contact layer are 2 mm and 0.5 mm, respectively.

The module testing and stimulation procedures are similar to previous reports.[3,4] The eight-couple p- and n-type legs were alternately positioned onto the Cu substrate with dimensions of 18 mm × 15 mm × 1 mm, where 0.21 mm thick Cu patterns were printed onto the 0.08 mm thick heat conducting polymer film (TSS Co., Ltd.). The legs were interconnected by the Cu electrodes of 5 mm × 2 mm × 1 mm. Liquid In-Ga eutectic alloy was smeared between legs and Cu interconnecting electrodes to reduce the electrical and thermal contact resistances. Two thick Cu leading wires and two thin Cu wires were soldered to the Cu pattern to supply the electrical current and measure the terminal voltage, respectively.

The electrical power output and conversion efficiency of fabricated modules were measured using a hot-side temperature of 373 K, 423 K, 473 K, 523 K, 573 K, and 593 K in a vacuum (10^{-2}-10^{-3} Pa) on a home-built testing system. The cold-side temperature was maintained at 278 K. The modules were mounted between AlN ceramic plates. The heater, AlN ceramic plates, module, and Cu blocks were pressed by a pneumatic cylinder under a uniaxial pressure of 1 MPa to reduce the electrical and thermal contact resistances. Peltier cooling devices were placed at the bottom of Cu base to maintain the cold-side temperature at 278 K. A graphite sheet (110 mm thick, Grafoil) and thermal grease (KS-613, Shin-Etsu Silicone) were used at hot side and at cold side, respectively, to reduce further the thermal contact resistances between the Cu blocks and AlN ceramic plates and between the AlN ceramic plates and themodule. The hot- and cold-side temperatures of the module, T_h and T_c, were measured by using thermocouples embedded in the AlN ceramic plates.

An oxygen-free Cu block with known thermal conductivity (κ_{Cu}) having a size of 15 mm × 15 mm × 60 mm was used as a heat flow meter. Six thin Pt resistance thermometers (Pt100, 1.05 mm diameter) were embedded in the Cu block at a vertical distance (LPt100) of 40 mm to each other in order to measure the temperature drop ΔT along the heat flow direction. The T_h and T_c of the Cu block were measured by their respective three Pt resistance thermometers. The heat dissipated from the cold side of the module (Q_{out}) was calculated in accordance with one-dimensional Fourier's law:

$Q_{out} = \kappa_{Cu} \triangle T (A_{Cu} / L_{Pt100})$ where A_{Cu} is cross-sectional area of Cu block.

A direct current electronic load (PLZ164WA, Kikusui Electronics) was connected to the module for supplying the electrical current to measure the electrical power output. The conversion efficiency was calculated using the following Equation:

$$\eta = \frac{P}{P + Q_{out}}$$

The uncertainty of heat flow is estimated to be within ±3%; therefore, the uncertainty for efficiency measurement is estimated to be the same (within ±3%).

The P_{max} and η_{max} of our fabricated modules were investigated by the home-made program (TEPS1D300). A geometrical model was built in the software interface to represent module with an identical dimension. The model was composed of n-type $Mg_{3.2}Sb_{1.5}Bi_{0.49}Te_{0.01}Cu_{0.01}$ with Fe contact layer, p-type $Mg_{0.99}Cu_{0.01}Ag_{0.97}Sb_{0.99}$ with Ag contact layer, and Cu interconnecting electrodes. It should be noted that electrical and thermal contact resistances between these interfaces, resistances of Cu electrodes, and radiation effects are not considered in the simulation model. The measured electrical and thermal transport properties (S, ρ, and κ_{total}) of n-type $Mg_{3.2}Sb_{1.5}Bi_{0.49}Te_{0.01}Cu_{0.01}$ and p-type $Mg_{0.99}Cu_{0.01}Ag_{0.97}Sb_{0.99}$ were used for simulation, while those for the Ag and Fe contact layers were assumed to be constant.

The terminal voltage V, electrical power output P, heat dissipation from the cold side of the module Q_{out}, and conversion efficiency η were displayed as functions of electric current I (**Figure S23**). The slope of the V-I curve approximately represents the internal resistance of the fabricated module (**Figure S23a**). The open-circuit voltage (V_{oc}), as the y intercept on the V-I curve, ideally corresponds to the Seebeck voltage (= $S\Delta T$) of 8-pairs n-type and p-type legs. The valve of P ($P = VI$) reaches a maximum under the condition of the matched impedance (**Figure S23b**). The maximum power output (P_{max}) increases from 0.1 W for T_h at 373 K to 1.15 W for T_h at 593 K. Q_{out} increases with the current (**Figure S23c**), as a result of the Peltier heating and Joule heating. The open-circuit heat flow (Q_{oc}), the y-intercept on the Q_{out}-I curve, refers to heat conduction through the legs along with possible heat leakage by radiation, resulting in the underestimated conversion efficiency. The maximum conversion efficiency η_{max} increases with increasing temperature (**Figure S23d**), *e.g.,* from 2.1% for T_h at 373 K to 7.3% for T_h at 593 K.

Computational methods

The total energy calculations based on the density functional theory (DFT) were performed using Vienna ab initio package (VASP)[5-8] with projector augmented wave (PAW)[9] pseudopotentials. The generalized gradient approximation functional with Perdew-Burke-Ernzerhof parametrization (GGA-PBE)[10] was chosen for the exchange and correlation potentials.

To search for likely interstitial sites in Mg_3Sb_2, we adopted Voronoi tessellation implemented in Pylada package.[11] We created three types of 3 × 3 × 2 supercell with a Cu-interstitial atom placed on the suggested interstitial sites. The modeled structures were fully relaxed without considering symmetry until the residual forces became less than 10^{-3} eV/Å, and then the most energetically stable structure was chosen for the following calculations. The cutoff energy was chosen as 350 eV, and 8 × 8 × 4 (primitive cell) and 3 × 3 × 2 (supercell with interstitial atom) *k*-point grids were used for the calculations of structure relaxation and electron localization function (ELF). The deformation potential for electrons, which is defined based on the energy change of the conduction band minimum (CBM) as $E_d^{\mathrm{CBM}} = \partial E^{\mathrm{CBM}}/(\partial a/a_0)$ (E^{CBM} and a_0 are the band energy of CBM and the equilibrium lattice constant, respectively), was calculated by varying the lattice constant ($0.990a_0$, $0.995a_0$, a_0, $1.005a_0$, and $1.010a_0$). Here, we used the energy level of the deep core state as the reference to determine the change of band energy.

The harmonic interatomic force constants, phonon density of states, group velocity, and three-phonon scattering phase space (SPS) were calculated using ALAMODE.[12] The SPS is given as

$$W_q^{\pm} = \frac{1}{N}\sum_{q',q''}\begin{Bmatrix} n_{q''} - n_{q'} \\ n_{q'} + n_{q''} + 1 \end{Bmatrix}\delta\left(\omega_q - \omega_{q'} \pm \omega_{q''}\right), (1)$$

where W_q^+ and W_q^- are the SPS corresponding to absorption and emission processes of phonon mode q, respectively. Here, the variable q is defined by $q = (\boldsymbol{q}, j)$ and $-q = (-\boldsymbol{q}, j)$ where $\boldsymbol{q}$ and j are the wave vector and the branch index of phonon modes. n_q is the Bose-Einstein distribution function.

SUPPLEMENTAL FIGURES

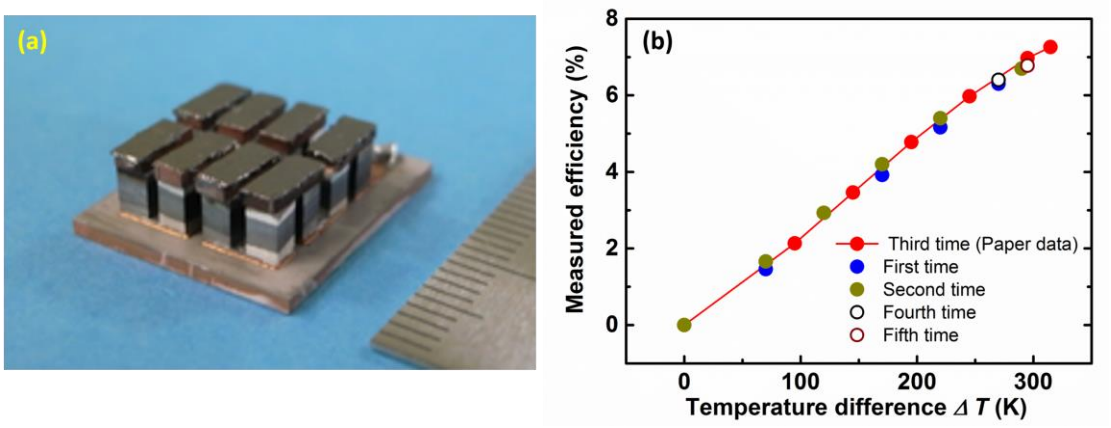

Figure S1. (a) The photo of our fabricated module and (b) the measured conversion efficiency of our module during the cycling test

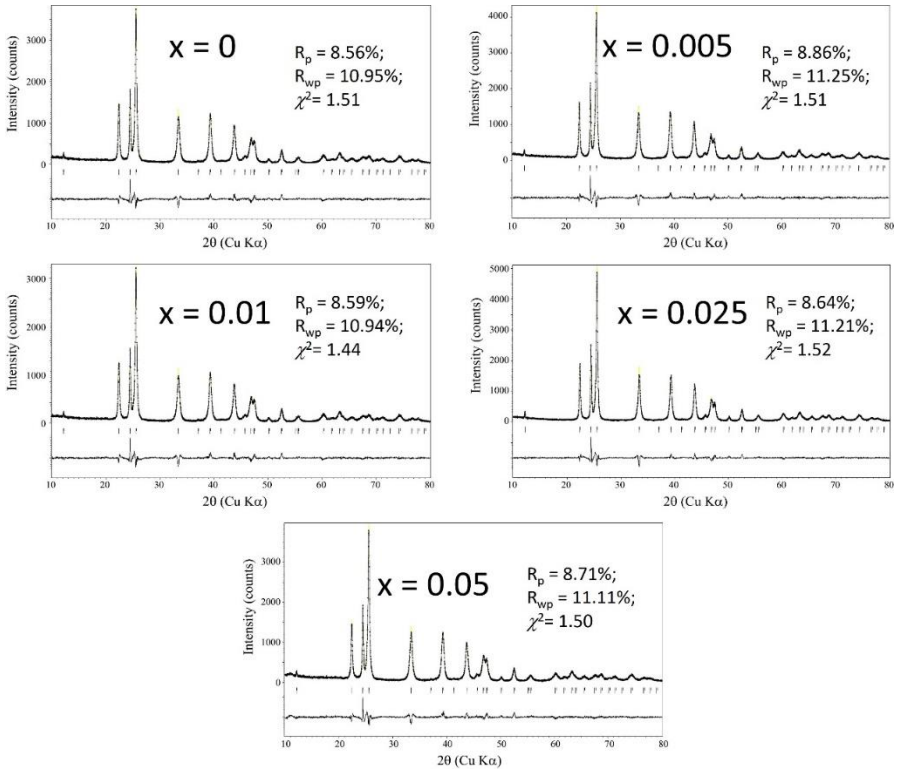

Figure S2. The XRD refinement results of $Mg_{3.2}Sb_{1.5}Bi_{0.49}Te_{0.01}Cu_x$ (x = 0, 0.005, 0.01, 0.025, and 0.05) samples. No second phases, *e.g.*, MgO or Mg_2Cu, are observed within the XRD detection limit.

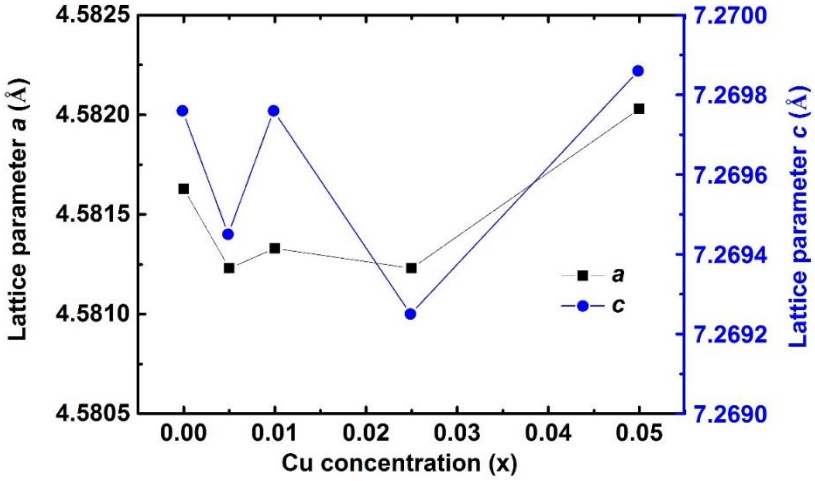

Figure S3. The calculated lattice parameters *a* and *c* as a function of Cu concentration

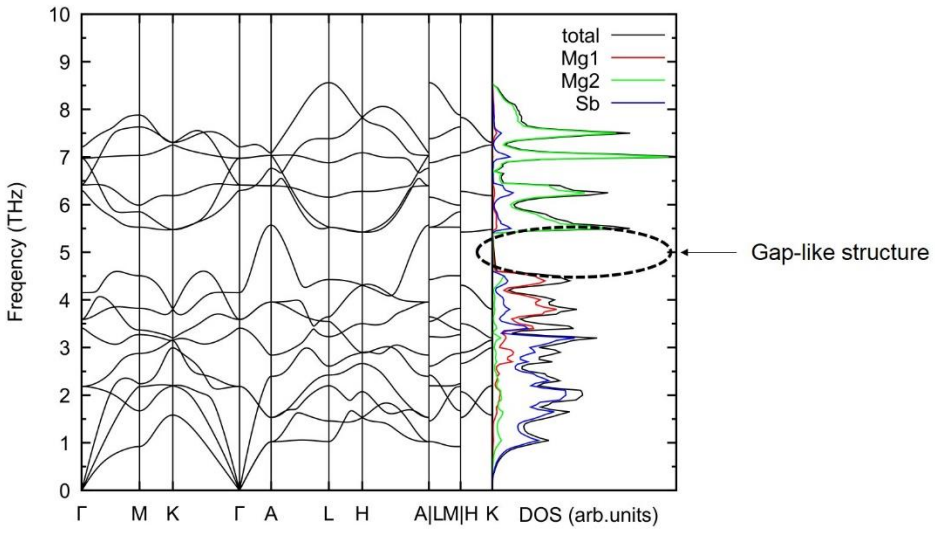

Figure S4. The phonon dispersion and phonon density of states (DOS) of pristine Mg_3Sb_2

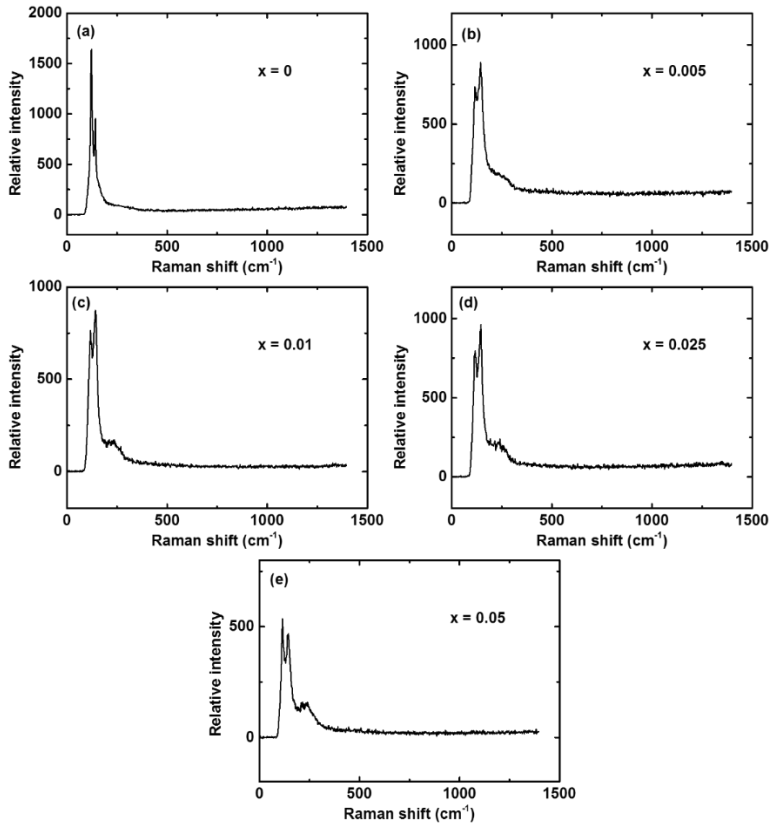

Figure S5. Room-temperature Raman spectra of $Mg_{3.2}Sb_{1.5}Bi_{0.49}Te_{0.01}Cu_x$ (x = 0, 0.005, 0.01, 0.025, and 0.05)

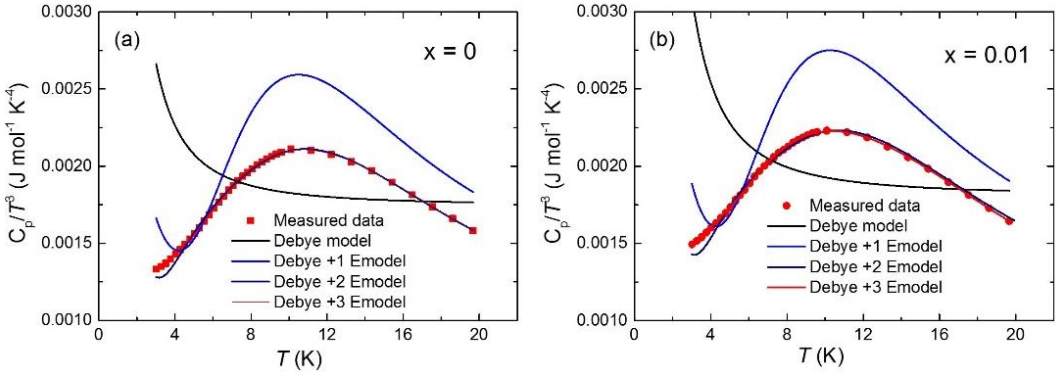

Figure S6. Temperature-dependent heat capacity C_p, depicted as C_p/T^3 as a function of T for $Mg_{3.2}Sb_{1.5}Bi_{0.49}Te_{0.01}Cu_x$ (x = 0 and 0.01)

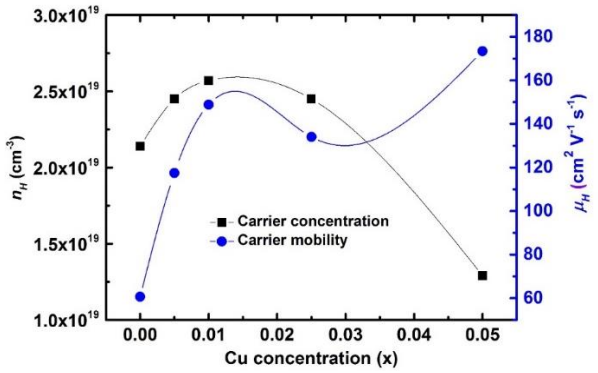

Figure S7. Hall carrier concentration n_H and carrier mobility μ_H of $Mg_{3.2}Sb_{1.5}Bi_{0.49}Te_{0.01}Cu_x$ (x = 0, 0.005, 0.01, 0.025, and 0.05) as a function of Cu concentration

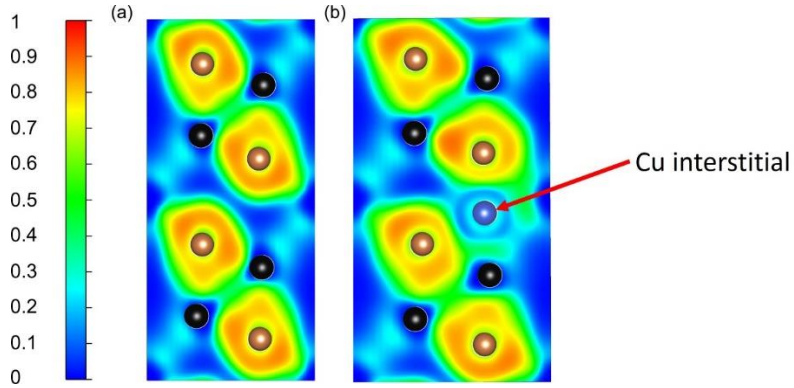

Figure S8. Comparison of electron localization function (ELF) image between pristine Mg_3Sb_2 on the plane of $(2\bar{1}0)$ and Mg_3Sb_2 with Cu interstitial

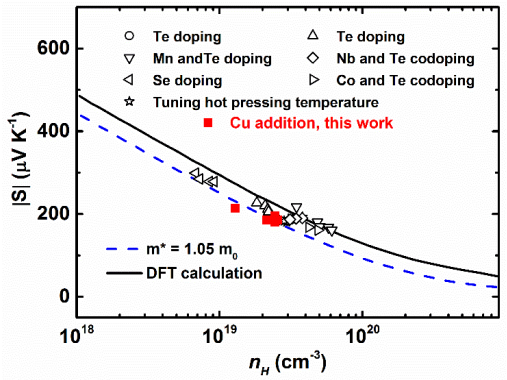

Figure S9. The absolute value of room-temperature Seebeck coefficients of $Mg_{3.2}Sb_{1.5}Bi_{0.5}$ based materials as a function of carrier concentration n_H [13-20]

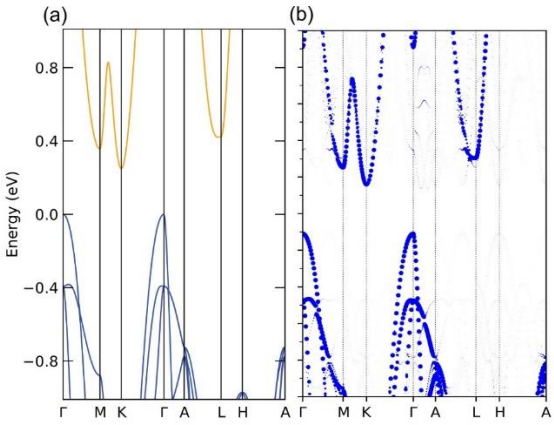

Figure S10. (a) Electronic band structure of pristine Mg_3Sb_2 and (b) the unfolded band structure of Mg_3Sb_2 with Cu interstitial

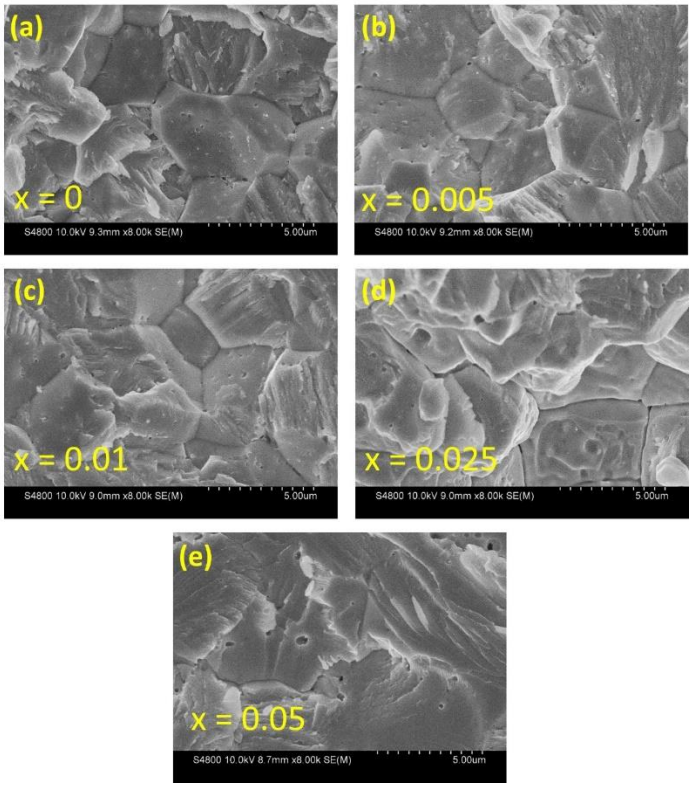

Figure S11. (a)-(e) Scanning electron microscopy (SEM) image of the fresh fracture surface of $Mg_{3.2}Sb_{1.5}Bi_{0.49}Te_{0.01}Cu_x$ (x = 0, 0.005, 0.01, 0.025, and 0.05), respectively. (f) The polish surface and the corresponding energy dispersive X-ray spectroscopy (EDS) mapping result of $Mg_{3.2}Sb_{1.5}Bi_{0.49}Te_{0.01}Cu_{0.01}$. Due to the low concentration of both Te and Cu elements, they are beyond the facility analysis detection.

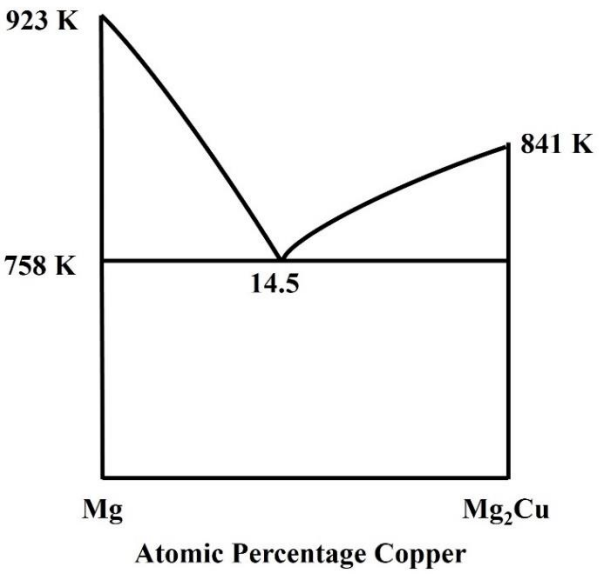

Figure S12. Mg-Cu binary Phase diagram[21]

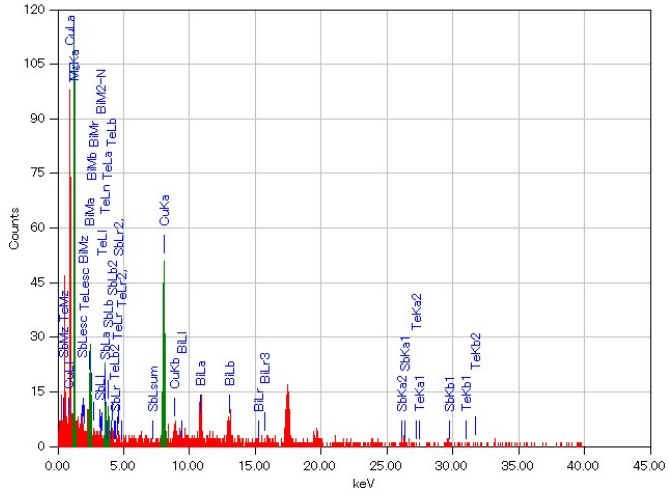

Figure S13. The STEM-EDS spectrum around the triple junction area of $Mg_{3.2}Sb_{1.5}Bi_{0.49}Te_{0.01}Cu_{0.01}$ sample, in which the obtained atomic percentage of Mg, Cu, Sb, Bi, Te are 53.2, 30.65, 9.97, 5.38, and 0.79, respectively. It should be noted that the measured signal of Sb and Bi arise from the contribution of the matrix since we chose a large square area to receive a high-intensity signal.

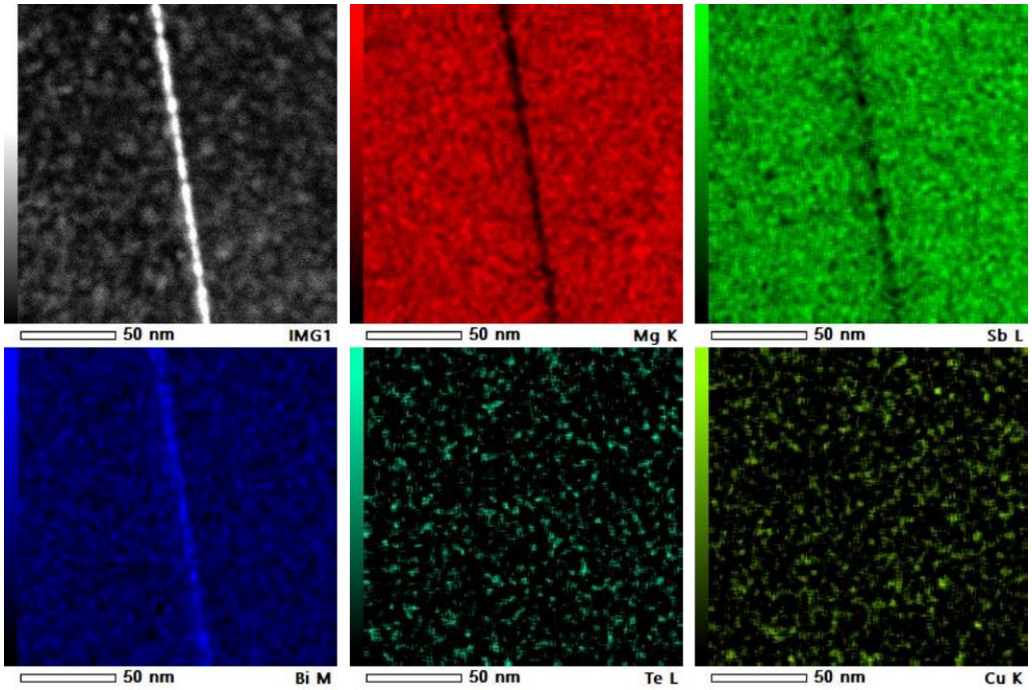

Figure S14. The HADDF-EDS mapping around a grain boundary in $Mg_{3.2}Sb_{1.5}Bi_{0.49}Te_{0.01}Cu_{0.01}$ sample

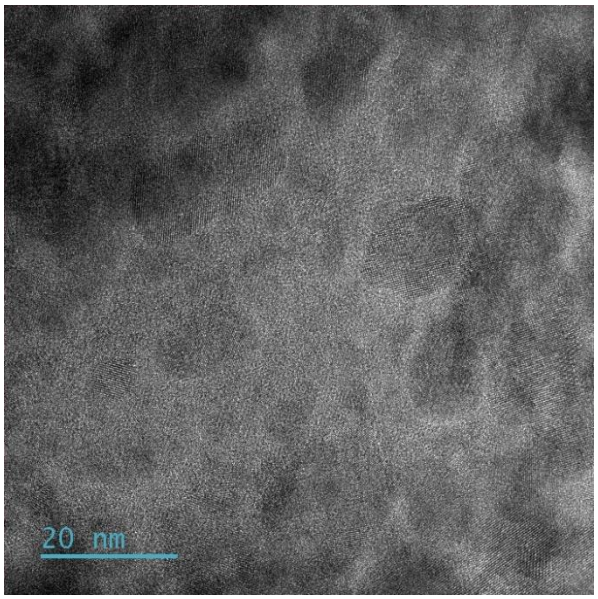

Figure S15. The HRTEM image showing the presence of nanoprecipates inside the grain of $Mg_{3.2}Sb_{1.5}Bi_{0.49}Te_{0.01}Cu_{0.01}$ sample

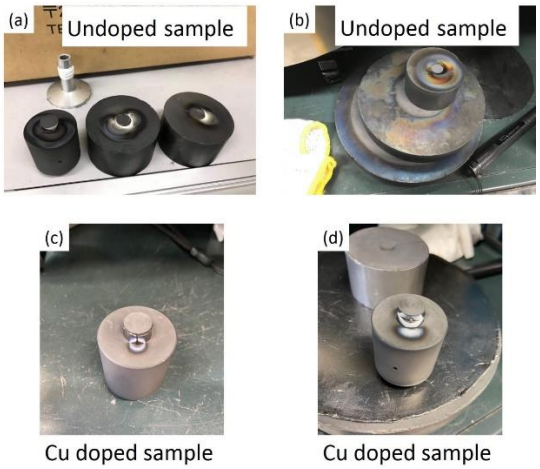

Figure S16. (a) and (b) Photos of graphite dies after sintering for $Mg_{3.2}Sb_{1.5}Bi_{0.49}Te_{0.01}$; (c) and (d) Photos of graphite dies after sintering for $Mg_{3.2}Sb_{1.5}Bi_{0.49}Te_{0.01}Cu_{0.05}$

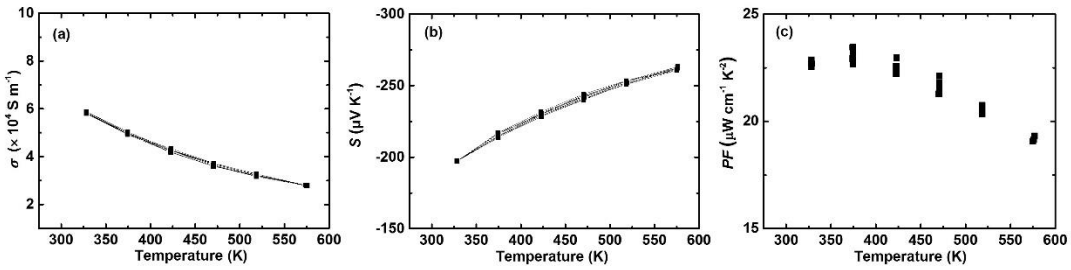

Figure S17. The 5-times cycling result of electrical transport properties of $Mg_{3.2}Sb_{1.5}Bi_{0.49}Te_{0.01}Cu_{0.01}$. (a), (b), and (c) Temperature dependent electrical conductivity σ, Seebeck coefficient S, and power factor PF, respectively.

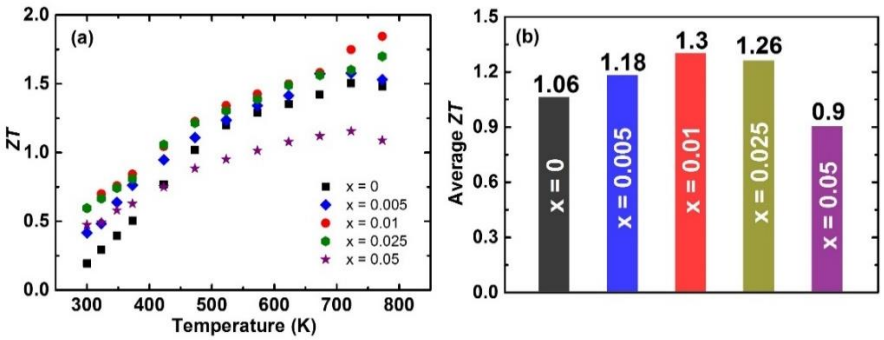

Figure S18. (a) Temperature dependent ZT of $Mg_{3.2}Sb_{1.5}Bi_{0.49}Te_{0.01}Cu_x$ (x = 0, 0.005, 0.01, 0.025, and 0.05). (b) The corresponding average ZT from 300 K to 773 K

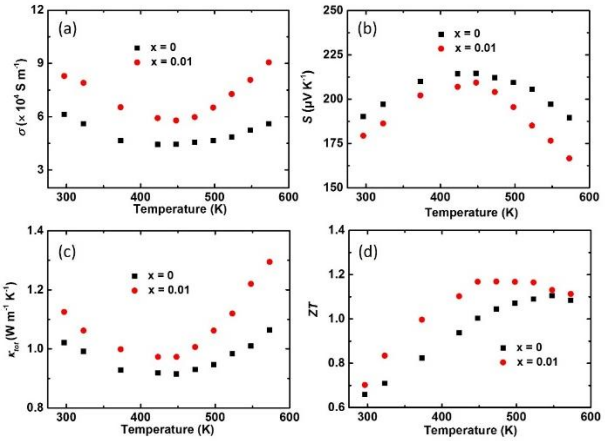

Figure S19. Thermoelectric properties of $Mg_{1-x}Cu_xAg_{0.97}Sb_{0.99}$ (x = 0 and 0.01). (a), (b), (c) and (d) Temperature dependent electrical conductivity σ, Seebeck coefficient S, , total thermal conductivity κ_{tot}, and ZT, respectively. (Submitted)

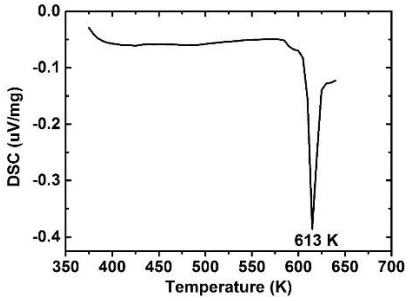

Figure S20. DSC measurement result of $Mg_{0.99}Cu_{0.01}Ag_{0.97}Sb_{0.99}$

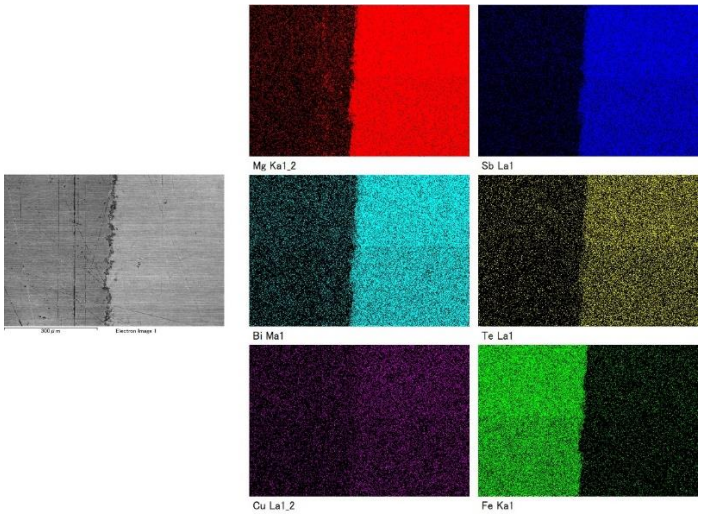

Figure S21. The polished surface morphology and the corresponding EDS mapping of n-type $Mg_{3.2}Sb_{1.5}Bi_{0.49}Te_{0.01}Cu_{0.01}$ leg

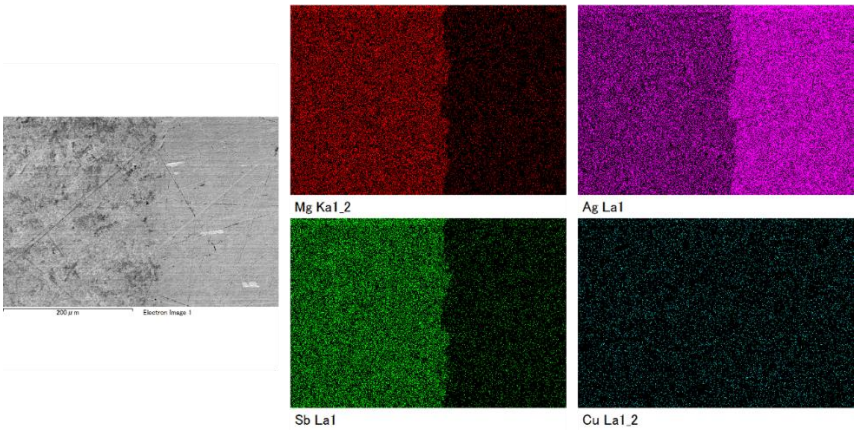

Figure S22. The polished surface morphology and the corresponding EDS mapping of p-type $Mg_{0.99}Cu_{0.01}Ag_{0.97}Sb_{0.99}$ leg

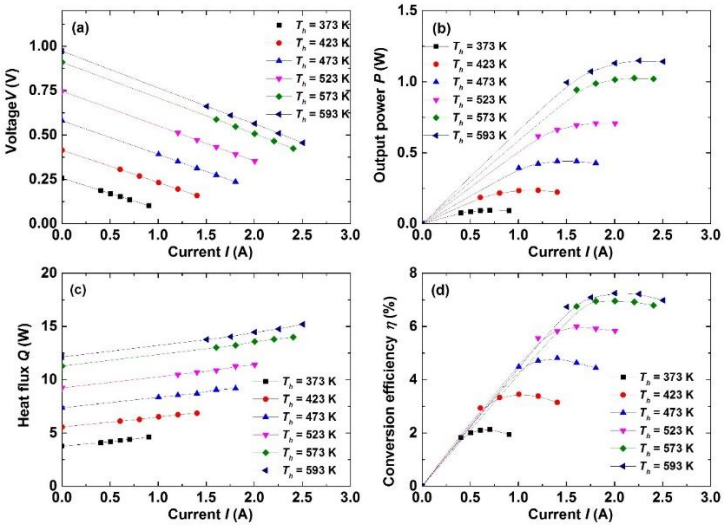

Figure S23. Power-generating properties of $Mg_3Sb_{1.5}Bi_{0.5}$/MgAgSb module. (a)-(d) Measured terminal voltage (V), electrical power output (P), heat dissipation from the cold side of the module (Q_{out}), and conversion efficiency (η) as functions of electrical current I, respectively. The hot-side temperature (T_h) was set as 373 K, 423 K, 473 K, 523 K, 573 K, 593 K, respectively, while the cold-side temperature T_c was maintained at 278 K.

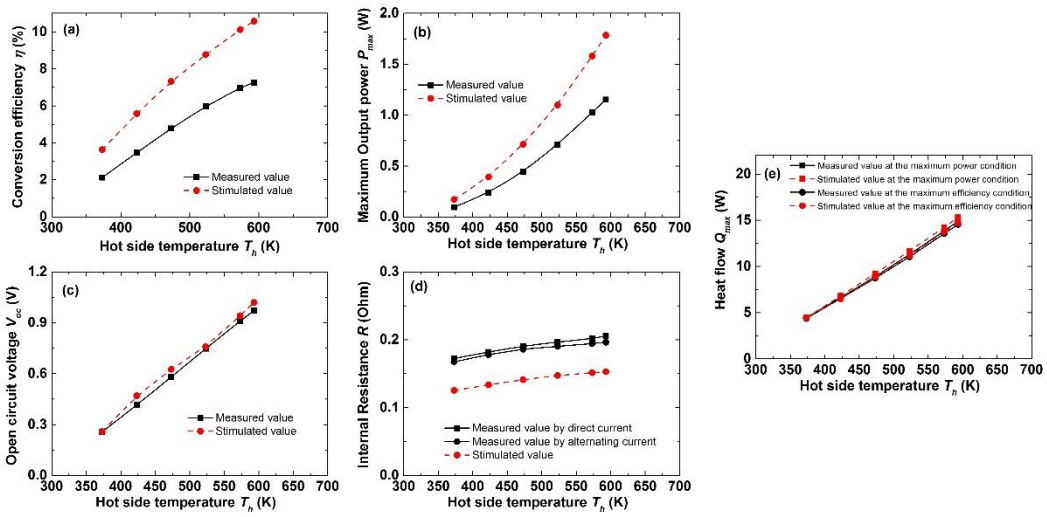

Figure S24. Measured and stimulated power-generating properties of $Mg_3Sb_{1.5}Bi_{0.5}$/MgAgSb module. (a)-(e) Conversion efficiency (η), maximum output power (P_{max}), open circuit voltage V_{oc}, internal resistance R, and heat flow Q_{max} as a function of hot-side temperature, respectively.

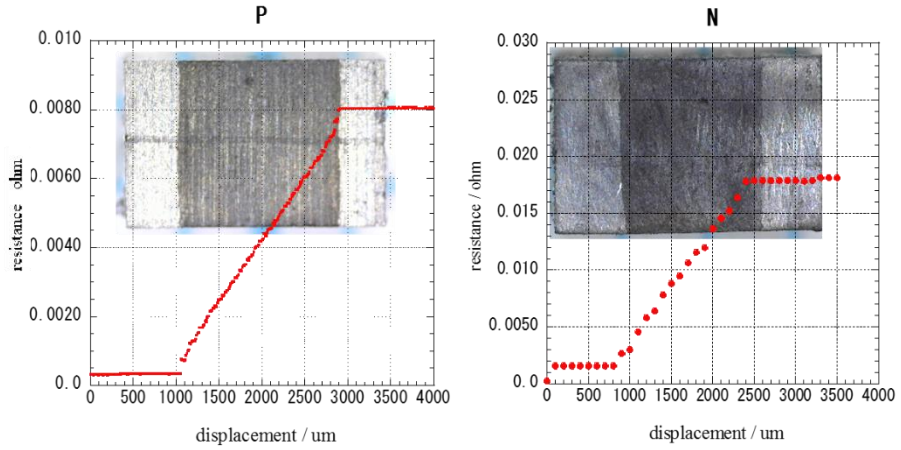

Figure S25. Room-temperature material resistance of p-type MgAgSb/Ag and n-type $Mg_{3.2}Sb_{1.5}Bi_{0.5}$/Fe interface, indicating the obvious "jump" over the interface

SUPPLEMENTAL TABLES

Table S1. The longitudinal sound velocity v_l, transverse sound velocity v_t, average sound velocity v_a, Debye temperature Θ_D, and Grüneisen parameter γ of $Mg_{3.2}Sb_{1.5}Bi_{0.49}Te_{0.01}$ and $Mg_{3.2}Sb_{1.5}Bi_{0.49}Te_{0.01}Cu_{0.01}$

Composition	v_l (m/s)	v_t (m/s)	v_a (m/s)	Θ_D (K)	γ
$Mg_{3.2}Sb_{1.5}Bi_{0.49}Te_{0.01}$	3811	1836	2064	207	2.12
$Mg_{3.2}Sb_{1.5}Bi_{0.49}Te_{0.01}Cu_{0.01}$	3587	1719	1932	194	2.14

Table S2. Fitting parameters in the Debye-Einstein model for $Mg_{3.2}Sb_{1.5}Bi_{0.49}Te_{0.01}Cu_x$ (x = 0 and 0.01)

Sample	δ	β	A1	Θ_{E1}	A2	Θ_{E2}	A3	Θ_{E3}
	mJ mol^{-1} K^{-2}	mJ mol^{-1} K^{-4}		K		K		K
x = 0	3.59	0.55	0.36	21.66	5.49	47.41	16.18	82.34
x = 0.01	3.74	0.65	0.26	21.40	4.55	46.50	14.08	79.10

Table S3. The measured atomic percentage of synthesized $Mg_{3.2}Sb_{1.5}Bi_{0.49}Te_{0.01}Cu_x$ by SEM + EDS

Nomimal composition	Mg	Sb	Bi
$Mg_{3.2}Sb_{1.5}Bi_{0.49}Te_{0.01}$	57.77	32.29	9.94
$Mg_{3.2}Sb_{1.5}Bi_{0.49}Te_{0.01}Cu_{0.005}$	58.72	31.42	9.86
$Mg_{3.2}Sb_{1.5}Bi_{0.49}Te_{0.01}Cu_{0.01}$	59.24	30.73	10.03
$Mg_{3.2}Sb_{1.5}Bi_{0.49}Te_{0.01}Cu_{0.025}$	59.16	31.18	9.66
$Mg_{3.2}Sb_{1.5}Bi_{0.49}Te_{0.01}Cu_{0.05}$	59.49	30.50	10.01

Reference

1 Zhao, H.Z., Sui, J.H., Tang, Z.J., Lan, Y.C., Jie, Q., Kraemer, D., McEnaney, K., Guloy, A., Chen, G., and Ren, Z.F. (2014). High thermoelectric performance of MgAgSb-based materials. Nano Energy *7*, 97-103.

2 Liu, Z.H., Wang, Y.M., Mao, J., Geng, H.Y., Shuai, J., Wang, Y.X., He, R., Cai, W., Sui, J.H., and Ren, Z.F. (2016). Lithium Doping to Enhance Thermoelectric Performance of MgAgSb with Weak Electron-Phonon Coupling. Adv. Energy Mater. *6*, 1502269.

3 Hu, X., Jood, P., Ohta, M., Kunii, M., Nagase, K., Nishiate, H., Kanatzidis, M.G., and Yamamoto, A. (2016). Power generation from nanostructured PbTe-based thermoelectrics: comprehensive development from materials to modules. Energy Environ. Sci. *9*, 517-529.

4 Jood, P., Ohta, M., Yamamoto, A., and Kanatzidis, M.G. (2018). Excessively doped PbTe with Ge-induced nanostructures enables high-efficiency thermoelectric modules. Joule *2*, 1339-1355.

5 Kresse, G., and Hafner, J. (1993). Ab initio molecular dynamics for liquid metals. Phys. Rev. B *47*, 558.

6 Kresse, G., and Hafner, J. (1994). Ab initio molecular-dynamics simulation of the liquid-metal–amorphous-semiconductor transition in germanium. Phys. Rev. B *49*, 14251.

7 Kresse, G., and Furthmüller, J. (1996). Efficient iterative schemes for ab initio total-energy calculations using a plane-wave basis set. Phys. Rev. B *54*, 11169.

8 Kresse, G., and Furthmüller, J. (1996). Efficiency of ab-initio total energy calculations for metals and semiconductors using a plane-wave basis set. Computational materials science *6*, 15-50.

9 Blöchl, P.E. (1994). Projector augmented-wave method. Phys Rev B *50*, 17953.

10 Perdew, J.P., Burke, K., and Ernzerhof, M. (1996). Generalized gradient approximation made simple. Phys. Rev. Lett. *77*, 3865.

11 Goyal, A., Gorai, P., Peng, H., Lany, S., and Stevanović, V. (2017). A computational framework for automation of point defect calculations. Computational Materials Science *130*, 1-9.

12 Tadano, T., Gohda, Y., and Tsuneyuki, S. (2014). Anharmonic force constants extracted from first-principles molecular dynamics: applications to heat transfer simulations. J. Phys. Condens. Matter. *26*, 225402.

13 Tamaki, H., Sato, H.K., and Kanno, T. (2016). Isotropic Conduction Network and Defect Chemistry in $Mg_{3+\delta}Sb_2$-Based Layered Zintl Compounds with High Thermoelectric Performance. Adv. Mater. *28*, 10182-10187.

14 Mao, J., Shuai, J., Song, S.W., Wu, Y., Dally, R., Zhou, J.W., Liu, Z.H., Sun, J.F., Zhang, Q.Y., dela Cruz, C*., et al.* (2017). Manipulation of ionized impurity scattering for achieving high thermoelectric performance in n-type Mg_3Sb_2-based materials. Proc. Natl. Acad. Sci. USA *114*, 10548-10553.

15 Mao, J., Wu, Y.X., Song, S.W., Shuai, J., Liu, Z.H., Pei, Y.Z., and Ren, Z.F. (2017). Anomalous electrical conductivity of n-type Te-doped $Mg_{3.2}Sb_{1.5}Bi_{0.5}$. Mater. Today Phys. *3*, 1-6.

16 Mao, J., Wu, Y.X., Song, S.W., Zhu, Q., Shuai, J., Liu, Z.H., Pei, Y.Z., and Ren, Z.F. (2017). Defect Engineering for Realizing High Thermoelectric Performance in n-Type Mg_3Sb_2-Based Materials. ACS Energy Letters *2*, 2245-2250.

17 Shuai, J., Mao, J., Song, S.W., Zhu, Q., Sun, J.F., Wang, Y.M., He, R., Zhou, J.W., Chen, G., Singh, D.J.*, et al.* (2017). Tuning the carrier scattering mechanism to effectively improve the thermoelectric properties. Energy Environ. Sci. *10*, 799-807.

18 Zhang, J.W., Song, L.R., Mamakhel, A., Jørgensen, M.R.V., and Iversen, B.B. (2017). High-performance low-cost n-type Se-doped Mg_3Sb_2-based Zintl compounds for thermoelectric application. Chem. Mater. *29*, 5371-5383.

19 Chen, X.X., Wu, H.J., Cui, J., Xiao, Y., Zhang, Y., He, J.Q., Chen, Y., Cao, J., Cai, W., Pennycook, S.J.*, et al.* (2018). Extraordinary thermoelectric performance in n-type manganese doped Mg_3Sb_2 Zintl: High band degeneracy, tuned carrier scattering mechanism and hierarchical microstructure. Nano Energy *52*, 246-255.

20 Zhang, J., Song, L., Pedersen, S.H., Yin, H., Hung, L.T., and Iversen, B.B. (2017). Discovery of high-performance low-cost n-type Mg_3Sb_2-based thermoelectric materials with multi-valley conduction bands. Nat. Commun. *8*, 13901.

21 Nayeb-Hashemi, A., and Clark, J. (1984). The Cu-Mg (copper-magnesium) system. Bulletin of Alloy Phase Diagrams *5*, 36-43.